

# Report on Instrumentation and Methods for In-Situ Measurements of the Secondary Electron Yield in an Accelerator Environment

W. H. Hartung, D. M. Asner<sup>1</sup>, J. V. Conway, C. A. Dennett<sup>2</sup>, S. Greenwald, J.-S. Kim<sup>3</sup>, Y. Li, T. P. Moore, V. Omanovic, M. A. Palmer<sup>4</sup>, C. R. Strohman

*Cornell Laboratory for Accelerator-based ScienceS and Education, Cornell University, Ithaca, New York, USA*

## Abstract

The achievable beam current and beam quality of a particle accelerator can be limited by the build-up of an electron cloud (EC) in the vacuum chamber. Secondary electron emission from the walls of the vacuum chamber can contribute to the growth of the electron cloud. An apparatus for in-situ measurements of the secondary electron yield (SEY) of samples in the vacuum chamber of the Cornell Electron Storage Ring (CESR) has been developed in connection with EC studies for the CESR Test Accelerator program (CESRTA). The CESRTA in-situ system, in operation since 2010, allows for SEY measurements as a function of incident electron energy and angle on samples that are exposed to the accelerator environment, typically 5.3 GeV counter-rotating beams of electrons and positrons. The system was designed for periodic measurements to observe beam conditioning of the SEY with discrimination between exposure to direct photons from synchrotron radiation versus scattered photons and cloud electrons. The SEY chambers can be isolated from the CESR beam pipe, allowing us to exchange samples without venting the CESR vacuum chamber. Measurements so far have been on metal surfaces and EC-mitigation coatings. The goal of the SEY measurement program is to improve predictive models for EC build-up and EC-induced beam effects. This report describes the CESRTA in-situ SEY apparatus, the measurement tool and techniques, and iterative improvements therein.

## Contents

<b>1</b>	<b>Introduction</b>	<b>2</b>	<b>4</b>	<b>Measurement Method: Phase I</b>	<b>8</b>
<b>2</b>	<b>Apparatus</b>	<b>3</b>	<b>5</b>	<b>Measurement Method: Issues and Phase II Improvements</b>	<b>8</b>
2.1	Storage Ring Environment . . . . .	3	5.1	Ensuring Direct Photon Bombardment . . . . .	9
2.2	In-Situ SEY Stations . . . . .	4	5.2	Mitigation of Electron Gun Current Drift . . . . .	10
2.3	Samples . . . . .	5	5.3	Reduction of Charging and Parasitic Conditioning	11
2.4	Sample Exchange . . . . .	5	5.4	Leakage Current: Mitigation . . . . .	12
2.5	Magnetic Shielding . . . . .	5	5.5	Leakage Current: Measurement . . . . .	13
2.6	Electron Gun . . . . .	6	5.6	Transient Current: Mitigation . . . . .	13
2.7	Off-Line SEY Station . . . . .	6	5.7	Energy Resolution and Segmentation . . . . .	13
<b>3</b>	<b>SEY Measurement: Basics</b>	<b>6</b>	5.8	Improved Spatial Resolution and Range . . . . .	14
3.1	Secondary Electron Yield . . . . .	6	5.9	Spatial Resolution: Time Control and Hand-Shaking . . . . .	15
3.2	Indirect SEY Measurement . . . . .	6	5.10	Time Control: Cross-Talk Avoidance . . . . .	15
3.3	Parasitic Conditioning During the SEY Measurement . . . . .	7	5.11	Final Measurement Procedure . . . . .	16
3.4	Electron Gun Warm-Up; Gun Current . . . . .	7	<b>6</b>	<b>Data Analysis</b>	<b>17</b>
3.5	Electron Gun Deflection and Spot Size . . . . .	7	6.1	Energy Correction for Electrostatic Deflection . . . . .	17
3.6	Electrical System . . . . .	7	6.2	Correction for Sample Bias Voltage . . . . .	17
3.7	Data Acquisition . . . . .	8	6.3	Time-Dependent Correction of Leakage Current and Current Transients . . . . .	17
			6.4	Uncertainties . . . . .	19
			<b>7</b>	<b>Examples of SEY Results</b>	<b>19</b>
			7.1	SEY as a Function of Energy . . . . .	19
			7.2	Peak SEY as a Function of Vertical Position . . . . .	20
			7.3	Peak SEY as a Function of Incident Angle . . . . .	21
			7.4	Reproducibility . . . . .	21

<sup>1</sup>Present address: Pacific Northwest National Laboratory, Richland, WA

<sup>2</sup>Present address: Department of Nuclear Science and Engineering, Massachusetts Institute of Technology, Cambridge, MA

<sup>3</sup>Present address: Department of Electrical Engineering, Princeton University, Princeton, NJ

<sup>4</sup>Present address: Fermi National Accelerator Laboratory, Batavia, IL

<b>8 Conclusion</b>	<b>22</b>
<b>Acknowledgments</b>	<b>22</b>
<b>Appendix A Current Control and Measurement</b>	<b>22</b>
A.1 Electron Gun Current Control . . . . .	22
A.2 Electron Gun Current Modulation . . . . .	23
A.3 Current Measurement Parameters . . . . .	23
<b>Appendix B Parameters for Scanning the Energy, Focus, and Deflection</b>	<b>23</b>
B.1 Energy Segments . . . . .	23
B.2 Focus as a Function of Energy . . . . .	23
B.3 Deflection Parameters . . . . .	23
<b>Appendix C Collimation Slit Measurements</b>	<b>24</b>
C.1 Focus and Beam Spot Size . . . . .	24
C.2 Deflection Check . . . . .	24
<b>Appendix D Model for Time-Dependent Correction of Leakage Current and Current Transients</b>	<b>24</b>
D.1 Simple Measurements; Semi-Empirical Model .	24
D.2 Realistic Measurements; Additional Considerations . . . . .	25
D.3 Inferring Model Parameters from a Leakage Scan	27
<b>Appendix E Leakage Current Measurements</b>	<b>28</b>
E.1 Unmitigated Leakage Current: Correlation with Humidity; Time Dependence . . . . .	28
E.2 Mitigated Leakage Current: Long-Term Trends	29
<b>Appendix F Inter-System Timing for Simultaneous SEY Scans</b>	<b>30</b>
<b>References</b>	<b>30</b>

## 1. Introduction

Ideally, the beams in a particle accelerator propagate through a perfectly evacuated chamber. In reality, the vacuum chamber contains small amounts of residual gas, ions, and low-energy electrons. A number of processes can contribute to the build-up of the low-energy electrons: synchrotron-radiated photons striking the wall of the chamber can produce electrons by photo-emission; in the absence of synchrotron radiation, electrons can be produced by bombardment of the wall by the beam halo or ionisation of the residual gas by the beam. The electron population grows if the electrons hit the wall and produce secondary electrons with a probability greater than unity. In extreme cases, a large density of electrons can build up inside the beam chamber, causing disruption of the beam, heating of the chamber walls, and degradation of the vacuum. This is referred to as an “electron cloud” (EC).

Electron cloud effects were first observed in accelerators in the 1960s [1]. Positively charged beams are typically more prone to EC effects. Adverse effects from EC that have been observed in recent years include beam instabilities [2–10], degradation in the beam quality [7, 11, 12], and excess load to the

cryogenic system of cold-bore vacuum chambers [13]. Several accelerators have been modified to reduce the cloud density [5, 7, 12]. EC concerns led to EC mitigation features in the design of recent accelerators [10, 14] and proposed future accelerators [15–17]. Additional information on EC issues can be found in review papers such as [1, 14, 18].

The Cornell Electron Storage Ring (CESR) provides x-ray beams for users of the Cornell High Energy Synchrotron Source (CHESS) and serves as a test bed for future accelerators through the CESR Test Accelerator program (CESRTA) [19–21]. Major goals of the CESRTA program are to develop tools and techniques for operation at low beam emittance and to better understand electron cloud effects and their mitigation. The EC density is measured with multiple methods, including retarding field analyzers [22], shielded button electrodes [23], and microwave excitation [24]. The effectiveness of several types of coatings for EC mitigation has been measured by installing coated and instrumented chambers [22, 25].

In the presence of a stored beam and synchrotron radiation (SR), three surface phenomena are important in determining the build-up of the electron cloud: photo-emission of electrons; secondary emission of electrons; and scattering of photons. As indicated above, secondary emission is particularly important—since it is possible for a surface to release more electrons than are incident, secondary emission can make the electron cloud density grow, even without additional photons.

Surface properties are known to change with time in an accelerator vacuum chamber: this is referred to as “conditioning” or “beam scrubbing,” and is thought to be due to removal of surface contaminants by surface bombardment. The likely ammunition for surface bombardment includes SR photons radiated by the stored beam, scattered photons, electrons from the electron cloud, ions, and beam halo.

Because of the importance of secondary emission for electron cloud effects, a system was developed for in-situ measurements of the secondary electron yield (SEY) as a function of the energy and angle of the incident primary electrons. The goals of the CESRTA in-situ SEY studies included (i) measuring the SEY of surfaces that are commonly used for beam chambers; (ii) measuring the effect of beam conditioning; and (iii) comparing different materials and mitigation coatings. Samples were made from the same materials as one would find in an accelerator vacuum chamber, with similar surface preparation (sometimes called “technical surfaces” in the literature), as opposed to the pure materials and single-crystal samples which would be used for studies of intrinsic properties of solids.

The effect of exposure to an accelerator environment on the SEY of surfaces has been studied at Argonne [26], CERN [27–31], KEK [32, 33], and SLAC [34]. In-situ studies have been supplemented by bench measurements of conditioning by an electron beam [11, 26–29, 33, 35–42]. Additionally, sources of systematic error in SEY measurements and countermeasures have been studied at SLAC [43, 44].

In some of the other accelerator SEY conditioning studies, the samples were installed into the beam pipe for an extended period and then moved to a laboratory apparatus for SEY measurements. At Argonne, the removal of the samples required a

brief exposure to ambient air [26]. At PEP-II, the samples were moved under vacuum using a load-lock system [34].

Studies at CERN and KEK, on the other hand, used in-situ systems for the SEY measurements, so that the samples did not have to be removed from the tunnel [28, 29, 32, 33]. The in-situ SEY systems allow for more frequent measurements with fewer concerns about recontamination of the surface between beam exposure and the SEY measurement, but require a more elaborate system in the accelerator tunnel.

The SEY apparatus developed for CESR-TA was based on the system used in PEP-II at SLAC [34]. In lieu of the load-lock system used at SLAC, a more advanced vacuum system was designed, incorporating electron guns for in-situ SEY measurements. The measurements at CESR-TA are similar to the in-situ measurements at CERN and KEK, but with several differences: (i) we have studied a wider variety of materials than measured at CERN; (ii) we have done more frequent measurements than done at KEK to get a more complete picture of SEY conditioning as a function of time and beam dose; (iii) we have measured the dependence of SEY on position and angle of incidence. Systems similar to the CESR-TA stations were recently sent to Fermilab for EC studies in the Main Injector [45].

The CESR-TA in-situ samples are typically measured weekly during a regularly-scheduled 6-hour tunnel access. The SEY chamber design allows for samples to be exchanged rapidly; this can be done during the weekly access if needed. As was the case for the PEP-II studies, there are 2 samples at different angles, one in the horizontal plane, the other  $45^\circ$  below the horizontal plane. This allows us to compare conditioning by bombardment from direct SR photons in the middle of the horizontal sample versus bombardment by scattered photons and EC electrons elsewhere. Because the accelerator has down periods twice a year, we have been able to keep some samples in ultra-high vacuum after beam conditioning and observe the changes in SEY over several weeks, without exposure to air.

Models have been developed to describe the SEY as a function of incident energy and angle (for example, the probabilistic model of M. Furman and M. Pivi [46]). In the models, the secondary electrons are generally classified into 3 categories: “true secondaries,” which emerge with small kinetic energies; “rediffused secondaries,” whose energies are distributed from low to high, up to the energy of the incident primary electron; and “elastic secondaries,” which emerge with the same energy as the incident primary. The SEY models are used to predict the EC density and its effect on the accelerator beam. Our in-situ SEY measurement program is ultimately oriented toward developing more realistic SEY model parameters to allow for more accurate predictions of EC effects.

This report describes the apparatus and techniques developed for the in-situ SEY measurements, including the issues that were encountered and improvements that were made. For clarity, we will divide the stages of the measurement program chronologically into two parts, Phase I and Phase II, and further subdivide the latter into Phase IIa and Phase IIb. We describe the in-situ apparatus in Section 2. We discuss the basic features of the SEY measurements in Section 3. In Phase I, samples of 3 different materials were measured, starting in January

2010; the Phase I measurement techniques are summarised in Section 4. Improvements were made to the hardware and measurement techniques between January 2011 and August 2011. In Phase II, additional materials were measured in parallel with additional improvements to the techniques, with measurements starting in September 2011; the Phase II improvements are discussed in Section 5. Data analysis methods are discussed in Section 6. Examples of results are given in Section 7. The information herein is presented in a more compact form in a separate paper [47]. More details on the results for metals (aluminum, copper, and stainless steel) and films for EC mitigation (titanium nitride, amorphous carbon, and diamond-like carbon) can be found in other papers [21, 48–50].

## 2. Apparatus

There are two SEY stations to allow exposure of two samples to the accelerator environment. The SEY measurements are done in the accelerator tunnel with an electron gun while the samples remain under vacuum. Magnetic shielding is included to ensure that low-energy electrons from the gun are not deflected by stray magnetic fields. The samples are typically exchanged without removal of the SEY stations from the tunnel. An additional station outside the tunnel is used for supplementary measurements.

### 2.1. Storage Ring Environment

The Cornell Electron Storage Ring has a circumference of 768 meters. Electrons and positrons travel in opposite directions through a common beam pipe; both species can therefore affect the build-up of the electron cloud in the vacuum chamber. The in-situ SEY system is installed in a straight section called “L3,” which originally was the site of a detector for high-energy physics. The beam pipe in L3 is stainless steel and has a circular cross-section, with an inner diameter of 89 mm. The SEY beam pipe includes a retarding field analyser for measurements of the electron cloud density and energy distribution.

The SEY system is installed at the East end of L3; nearby bending magnets are located such that the SEY samples are exposed predominantly to SR from the electron beam, the closest bending magnet being about 6 m away. The photon flux at the SEY stations is lower than the ring-wide average. Most of the beam exposure of the SEY samples happens with CHSS conditions: a beam energy of 5.3 GeV, with beam currents of  $\sim 200$  mA for both electrons and positrons.

In an imperfect vacuum environment, beam scrubbing can be counteracted by recontamination of surfaces from the residual gas. Cold cathode ionisation gauges are used to monitor the pressure in the CESR beam pipe; the closest gauge is about 1 m from the SEY stations. The base pressure is generally  $\lesssim 1.3 \cdot 10^{-7}$  Pa. With CHSS beams, the pressure is typically  $\lesssim 6 \cdot 10^{-7}$  Pa after beam conditioning; after venting, the pressure can reach as high as  $\sim 10^{-4}$  Pa during initial beam conditioning. After beam conditioning,  $H_2$  is the dominant residual gas.



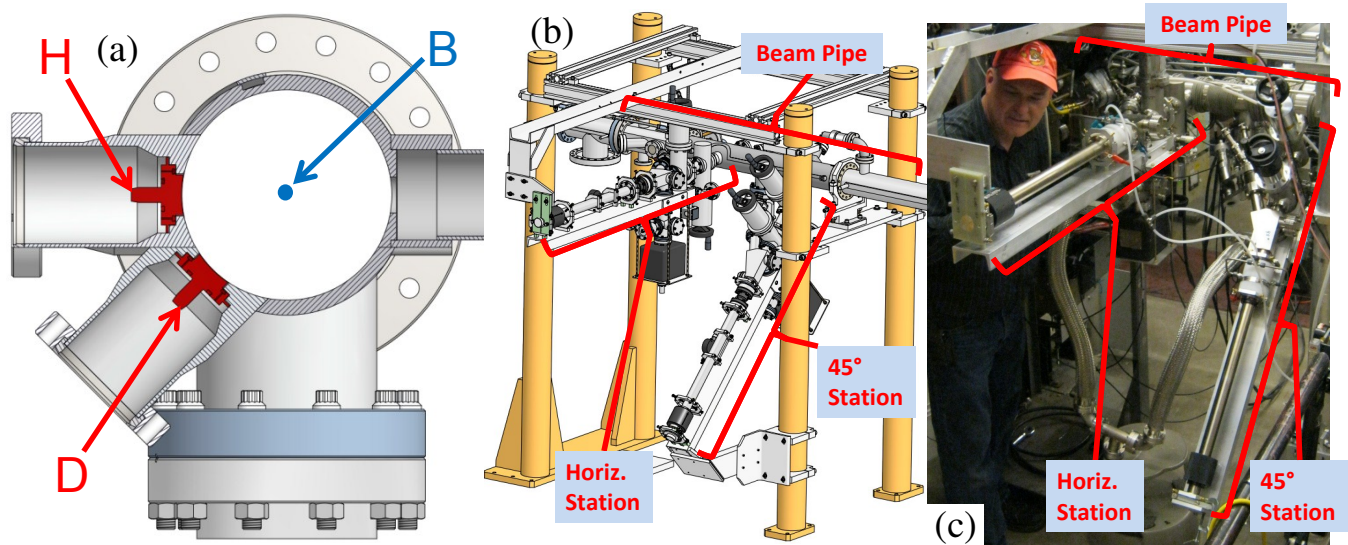


**Figure 1.** (a) “Beam’s eye” view of the SEY stations showing the beam (B), horizontal sample (H), and 45° sample (D). (b) Isometric drawing of the SEY stations, CESR beam pipe, and supports. (c) Photograph of the SEY stations in the tunnel. Note that (a) does not show the longitudinal separation of about 0.4 m between the samples, though this can be seen in (b) and (c).

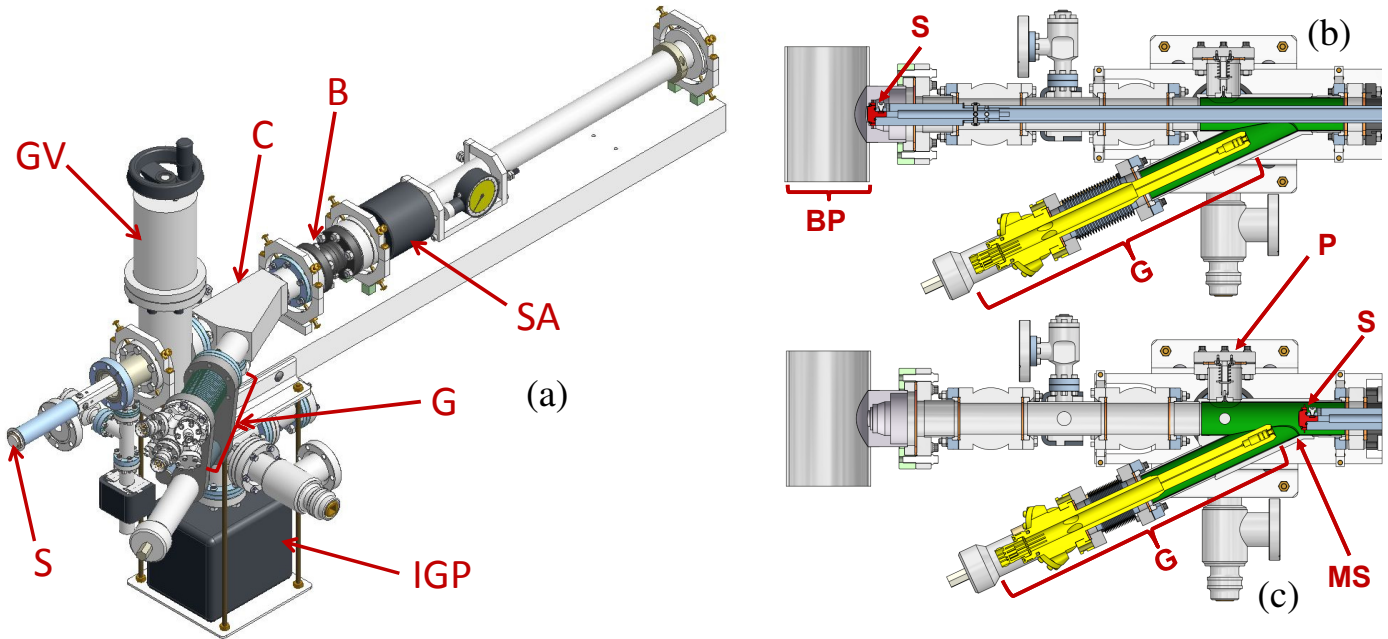


**Figure 2.** (a) Isometric view of one SEY station; the beam pipe and second gate valve are not shown. Cross-sectional views of in-situ station with (b) sample inserted in beam pipe and (c) sample retracted for SEY measurements. S: sample (red); G: electron gun (yellow); MS: magnetic shield (green); BP: beam pipe; P: port for sample exchange; C: vacuum crotch; B: ceramic break; SA: sample actuator; GV: gate valve; IGP: ion pump.

## 2.2. In-Situ SEY Stations

As shown in Figure 1a, the samples have a curved surface to match the circular beam pipe cross-section. Both samples are approximately flush with the inside beam pipe, with one sample positioned horizontally in the direct radiation stripe, and the other sample positioned at 45°, beneath the radiation stripe.

Figure 1b shows the SEY stations, with the equipment for moving the samples under vacuum and measuring the SEY; Figure 1c shows a photograph of the SEY stations in CESR.

More detailed drawings of one SEY station are shown in

Figure 2. A custom-designed vacuum “crotch” (made from 316LN stainless steel) provides an off-axis port for an electron gun, a pumping port, and a side port for sample exchange. The sample is mounted on a linear positioner with a magnetically-coupled manual actuator.<sup>5</sup> The sample and sample positioner are electrically isolated from the grounded beam pipe by a ceramic break.<sup>6</sup> The electron gun is at an angle of 25° from the

<sup>5</sup>Model DBLOM-26, Transfer Engineering, Fermont, CA.

<sup>6</sup>Model BRK-VAC5KV-275, Accu-Glass Products, Inc., Valencia, CA.

axis of the sample positioner. The gun is mounted on a compact linear positioner<sup>7</sup> so it can move out of the sample positioner's path when the sample is inserted into the beam pipe (Figure 2b).

When the sample is in the beam pipe for exposure to SR and the electron cloud (Figure 2b), force is applied to the actuator to ensure that the sample remains well seated. When the sample is in the SEY measuring position (Figure 2c), the gun is moved forward to make the gun-to-sample distance nominally 32.9 mm for the SEY measurements. Moving the gun forward allows for a smaller beam spot size on the sample and a larger range of incident angles.

The instrumentation for the SEY measurement is the same as that used in previous studies at SLAC [41]. A picoammeter<sup>8</sup> is used to measure the current from the sample; the sample dc bias is provided by a power supply internal to the picoammeter.

The vacuum in the SEY stations is maintained by ion pumps. The chambers also include titanium sublimation pumps in case additional pumping is needed. During the SEY measurements, one or both of two gate valves are closed to isolate the CESR vacuum system from the SEY chambers. Initially, hot-filament ionisation gauges were used to monitor the pressure in the SEY chambers. These were removed after the first few measurements on Al, as it appeared that the out-gassing from the filament might be affecting the SEY. Subsequently, we have used the ion pump current read-backs to infer the pressure in the SEY chambers. (We elected not to use cold cathode gauges, as these would have introduced stray magnetic fields if installed close enough to provide an accurate measurement of the pressure in the SEY chambers.) The ion pump read-backs indicate that the base pressure is less than  $10^{-7}$  Pa. With the electron gun on, the pressure increases slowly, but typically remains below  $10^{-6}$  Pa.

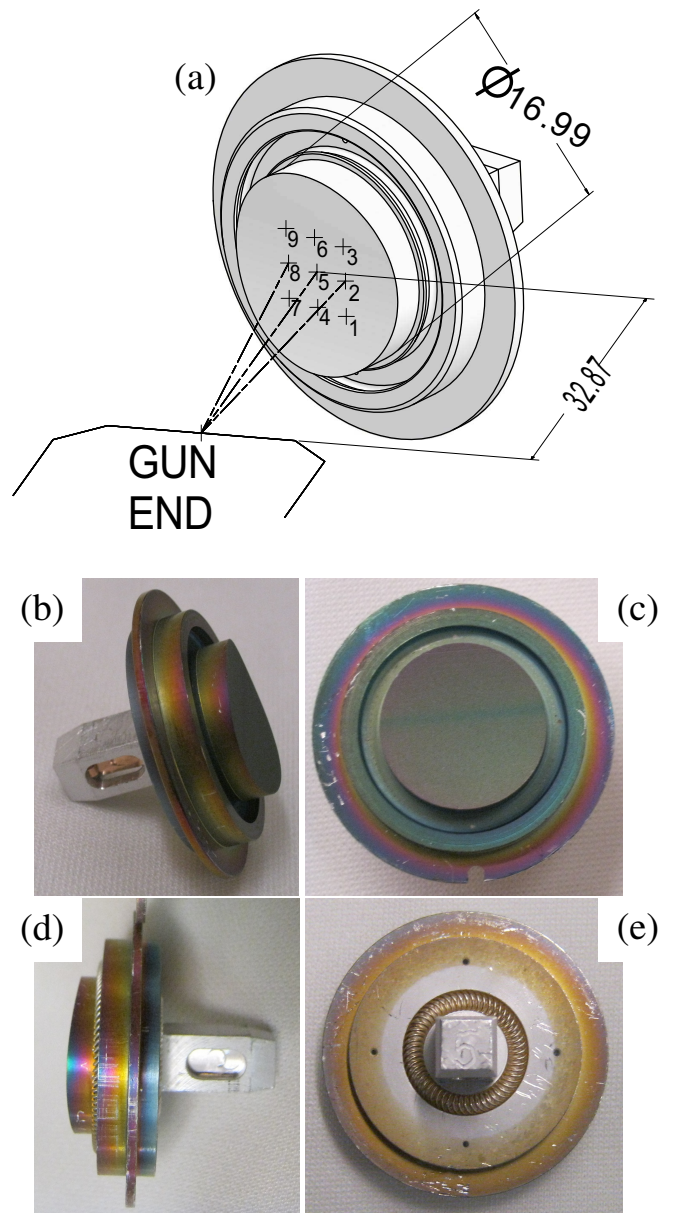
### 2.3. Samples

Figure 3 shows a drawing and photographs of the SEY sample. The samples are machined from bulk material; The design includes a groove in the back of the sample with a coiled ring spring (see Figure 3e) to ensure good electrical contact with the positioner rod which holds the sample.

The samples were solvent cleaned without mechanical polishing or etching, as typically surfaces in the CESR vacuum chamber are not polished prior to installation. Coatings (if any) were applied to the finished samples after solvent cleaning.

### 2.4. Sample Exchange

As shown in Figure 1, there are two gate valves between the beam pipe and the SEY chamber so that the sample can be changed without venting the beam chamber. (The second gate valve allows for the SEY chamber to be removed from the tunnel with the beam pipe and the sample still under vacuum). The SEY chamber has a special port for changing the samples in the tunnel (see Figure 2), with a custom-designed hole and patch in the magnetic shield. To minimize exposure to tunnel air, water vapor, and dust, nitrogen gas is flowed through the



**Figure 3.** (a) Isometric drawing of the SEY sample, showing the 3 by 3 grid of points where the SEY was measured in Phase I. The axis of the electron gun is inclined by  $25^\circ$  relative to the sample's surface normal. The diameter of the sample face and distance from the gun to the middle of the sample are indicated (dimensions in mm). (b-e) Photographs of a sample with a TiN coating: (c) front, (d) side, (e) back.

system when samples are exchanged; the exchange can be done with the flanges open for only a few minutes. When samples are exchanged with the  $N_2$  gas purge, the ultra-high vacuum recovers sufficiently to resume measurement within 24 hours. This makes it possible to change samples during a scheduled tunnel access over a regular CHESS running period.

### 2.5. Magnetic Shielding

At low energy (up to about 100 eV), the electrons can be deflected by up to a few millimeters by stray magnetic fields. To mitigate this problem, the electron gun and SEY sample are

<sup>7</sup>Model LMT-152, MDC Vacuum Products, LLC, Hayward, CA.

<sup>8</sup>Model 6487, Keithley Instruments, Inc., Cleveland, OH.

surrounded by a custom-made magnetic shield, shown in green in [Figure 2](#). The shield is inside the vacuum chamber and includes intersecting tubes for shielding of the sample positioner tube and the electron gun side port. The shield has a hole for the ion pumping port and, as described above, a patch for the sample exchange port. An internal shield has the advantage of being smaller, simpler and less susceptible to accidental damage than an external shield, at the cost of making the vacuum system more complicated. The shield was fabricated from nickel alloy mu-metal sheet of thickness 0.5 mm. The machining, forming, welding, and final heat treatment were done by a vendor<sup>9</sup> to our specifications. Metal finger stock was spot-welded to the outside of the shield for electrical grounding.

Measurements with a field probe indicated that the shield reduces the stray magnetic field to about 10  $\mu$ T or lower. To check the deflection with the shield present, we measured the transmission through a collimation electrode with a 1 mm vertical slit in front of the sample. At each electron beam energy, the beam was scanned across the slit using the gun's horizontal deflection electrode to determine whether compensation was needed to maximise the current through the slit. These measurements confirmed that the stray magnetic field is well shielded. Additional information about the collimation measurements can be found in [Appendix C](#).

The SEY station includes a metal rod to hold the sample (shown in light blue in [Figures 2b](#) and [2c](#)). The rod travels through the magnetic shield (as can be seen in [Figure 2](#)). We use an aluminum rod because we found that a stainless steel rod produced a small residual magnetic field.

## 2.6. Electron Gun

The electron gun<sup>10</sup> provides a dc beam with electrostatic acceleration to a maximum energy of 2 keV. The gun energy, current, deflection, and focusing are adjustable. The deflection is produced via horizontal and vertical electrostatic fields from paired electrodes. The focusing is produced by biasing a ring electrode. The focusing and deflection elements are internal to the electron gun. The gun's electron beam is produced by thermionic emission. Additional information on the control of the electron gun current can be found in [Section A.1](#).

## 2.7. Off-Line SEY Station

A duplicate SEY station was deployed outside the tunnel. This station is basically the same as the stations in L3, but it is not attached to a beam pipe and has the advantage of being accessible when the accelerator is running. This makes the off-line station useful for supplemental SEY measurements and debugging of measurement techniques.

## 3. SEY Measurement: Basics

In order to keep the stations compact enough for deployment in the tunnel, we use an indirect method to measure the secondary electron yield. Our basic measurement method is the same as has been used by SLAC [\[34, 41, 43\]](#) and other groups.

We measure the dependence of the SEY on (i) incident energy  $K$ , (ii) incident angle  $\theta$ , and (iii) impact position of the primary electrons ( $\theta$  = angle from the surface normal). For (i), we scan the electron gun energy. With the compact in-situ system, we cannot independently vary the angle and position. However, because of the curvature of the sample, scanning the beam spot vertically changes the position with little change in the incident angle, while scanning horizontally changes both the position and the angle (see [Figure 3a](#)). Hence, for (ii) and (iii), we scan the vertical and horizontal deflection of the electron gun. We make the beam spot size on the sample as small as possible for good position and angle resolution.

### 3.1. Secondary Electron Yield

The secondary electron yield is defined as the number of secondary electrons released from a surface divided by the number of incident primary electrons. In terms of current,

$$\text{SEY} = -\frac{I_s}{I_p}, \quad (1)$$

where  $I_p$  is the current of the primary electrons incident on the sample and  $I_s$  is the current of the secondary electrons released by the bombardment of primary electrons. The minus sign in [Equation \(1\)](#) is included because the primary and secondary electrons travel in opposite directions relative to the sample and hence we use a convention in which  $I_p$  and  $I_s$  have opposite signs. The SEY depends on the energy and angle of incidence of the primary electron beam.

### 3.2. Indirect SEY Measurement

The primary current  $I_p$  is measured by firing electrons at the sample with the electron gun and measuring the current from the sample with a positive bias voltage. A high positive bias voltage,  $V_b = +150$  V, is used to recapture secondaries produced by the primary beam, so that the net current due to secondaries is zero in the ideal case.

The current  $I_s$  due to secondary electrons is measured indirectly. The total current  $I_t$  is measured by again firing electrons at the sample, but with a low negative bias ( $V_b = -20$  V) on the sample to repel the secondaries. Since  $I_t = I_p + I_s$ , we calculate SEY as

$$\text{SEY} = -\frac{I_t - I_p}{I_p} = 1 - \frac{I_t}{I_p}. \quad (2)$$

If  $|I_p| > |I_s|$ , then  $I_p$  and  $I_t$  have the same sign,  $\text{SEY} < 1$ , and we observe a net flow of electrons from the gun to the sample when measuring  $I_t$ . If  $|I_p| < |I_s|$ , then  $I_p$  and  $I_t$  have opposite signs (because  $I_s$  and  $I_p$  have opposite signs),  $\text{SEY} > 1$ , and we observe a net flow of electrons away from the sample. In either case, current from the power supply flows through the picoammeter as needed to maintain the  $-20$  V bias on the sample.

<sup>9</sup>MuShield, Inc., Londonderry, NH.

<sup>10</sup>Gun: Model ELG-2; power supply: Model EGPS-1022C and EGPS-1022D; Kimball Physics, Inc., Wilton, NH. The insertion length of the electron gun is custom; the power supply design was modified for more stable output at low current.



A complication is that some secondary electrons may hit the walls of the vacuum chamber and produce additional electrons by secondary emission; hence, the negative sample bias should be large enough to prevent these electrons from returning to the sample. We chose  $V_b = -20$  V based on past measurements at SLAC [43].

Some SEY systems include an additional electrode to allow for a more direct measurement of  $I_s$ , for example the conical electrode system at KEK [51] and the energy analyser system used at SLAC [43]. Our in-situ setup cannot accommodate an extra electrode, so we cannot use such a method. We should also note that the positive bias for the  $I_p$  measurement in our indirect method is not able to retain elastic secondaries, so that the elastic contribution to the SEY is not fully accounted for, as has been pointed out previously [43].

### 3.3. Parasitic Conditioning During the SEY Measurement

To measure the SEY, we bombard the sample with electrons, which conditions the surface and changes the SEY. Since the goal is to observe conditioning by SR photons and the electron cloud, it is best to minimise conditioning by the electron gun during the SEY measurement [43]. A low electron gun current and a rapid measurement help to mitigate this problem, but the current must be large enough to measure and, as will be discussed below (see Section 5.6 in particular), waiting times are needed for stable conditions. As a result, we “park” the beam at a known position on the sample with a small beam spot size when we are not measuring  $I_t$ . We will discuss the issue of parasitic conditioning further in Section 5.3.

### 3.4. Electron Gun Warm-Up; Gun Current

Before starting the SEY measurement, we warm up the electron gun cathode, typically for 30 to 60 minutes. During the warm-up period, we set the gun energy to zero and the deflection to maximum to prevent the electron beam from reaching the sample. After warming up, we set the gun energy to 300 eV, deflect the beam to the parking point, and adjust the gun parameters (see Section A.1) to get the desired value of  $I_p$ . We typically observe a change in  $I_p$  with energy and a drift in  $I_p$  with time (see Figure 6 below). The latter is presumably due to the cathode temperature still changing slowly with time after the warm-up period (our choice of warm-up time is a compromise between the need for stable current and the need to finish the measurements in the available access time).

### 3.5. Electron Gun Deflection and Spot Size

Both the energy and the deflection of the electron gun are varied in the SEY scan. The deflection voltages must be scaled with energy to produce the same deflection angles for different energies (see Section B.3 for more information).

The focusing is set to minimize the beam spot size at the sample. The focusing voltage must be adjusted with energy, but the relationship is not linear. Separate measurements were done to find the parameters to produce the minimum spot size as a function of beam energy for the nominal gun-to-sample spacing (see Section B.2 for more information).

With the focus adjusted to minimise it, the estimated beam spot sizes for different energy ranges are as follows: slightly larger than 1 mm between 20 eV and 200 eV;  $\leq 0.75$  mm from 250 eV to 700 eV; about 1.2 mm at 1500 eV (increasing with energy between 800 eV and 1500 eV). For the 3 by 3 grid of Phase I measurements (Section 4), the approximate distance between adjacent grid points is 3.7 mm, so there is no overlap between grid points. For the higher resolution double grid developed in Phase II there is overlap between grid points over part of the energy range (as will be discussed in Section 5.8).

Collimation measurements provided the basis for the focus set point as a function of energy and the beam spot size estimates, as described in Appendix C.

### 3.6. Electrical System

An electrical schematic of the system is shown in Figure 4. As illustrated in Figure 5, the bias voltage is applied to the sample and positioner arm, which are separated by the ceramic break from the grounded SEY chamber, magnetic shield, and beam pipe. A nitrogen gas blanket is also shown in Figure 5; this will be discussed in Section 5.4.

Low-noise triaxial cables are used to bring the signals from the sample positioner arms to the picoammeters. The middle and outer conductors of the triaxial cable are connected to the SEY station ground and the inner conductor is connected to the sample. The picoammeter provides the biasing voltage, in addition to measuring the current: a small shielded circuit (connected to the picoammeter through another short triaxial cable) is used to connect the bias voltage from the picoammeter power supply. The outer conductors of the triaxial cables provide a shield for the signals carried by the middle and inner conductors. To avoid a ground loop, the outer conductors of the long and short triaxial cables are not connected to each other.

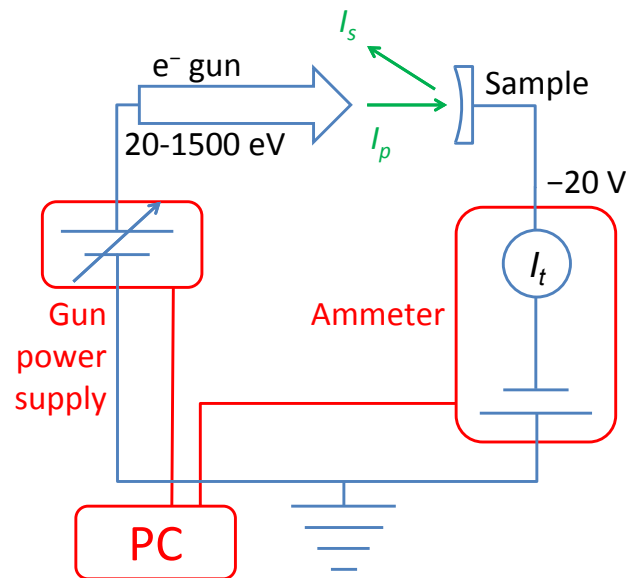


**Figure 4.** Electrical and data acquisition schematic, showing the sample with a negative bias to measure the total current ( $I_t = I_p + I_s$ ).

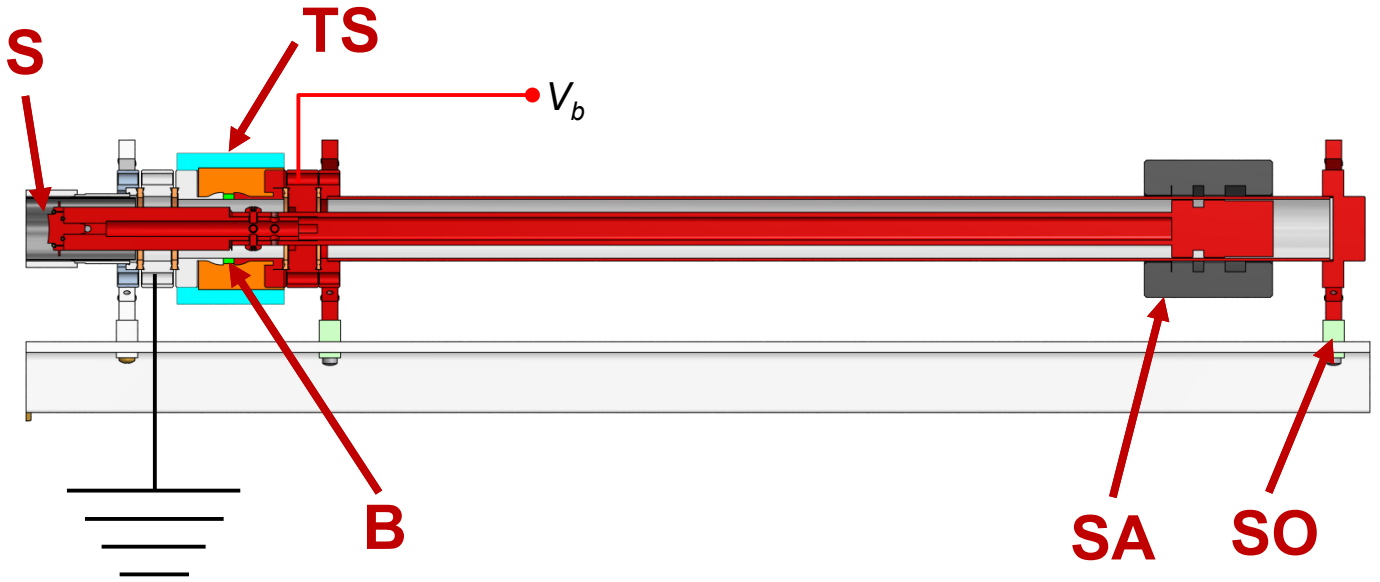


**Figure 5.** Side view of the SEY station, indicating portions which are biased in red. The chamber on the left is connected to the grounded beam pipe and support beam. The orange region represents the nitrogen gas blanket around the ceramic break. S: sample; B: ceramic break (green); SA: sample actuator; SO: stand-off (light green); TS: Teflon shell (light blue).

As can be seen in Figure 5, the sample positioner arms are not electrically shielded. As a result, activity that disturbs the air near the SEY stations produces noise in the current signals. In the tunnel, the area adjacent to the stations is roped off when SEY measurements are done to discourage visitors. With the off-line station, we minimise the presence of personnel in the room when doing SEY measurements.

As shown schematically in Figure 4, each station operates independently with a dedicated picoammeter, electron gun, electron gun power supply, and CPU, so that measurements on the horizontal and 45° sample can be done in parallel. The electronics are installed on a mobile equipment rack so that they can be removed when the accelerator is operating.

### 3.7. Data Acquisition

The SEY scans are automatic and are controlled by a data acquisition program (DAQP) implemented in LabVIEW.<sup>11</sup> The LabVIEW program incorporates existing software from Kimball Physics and Keithley for control and readout of the electron gun and picoammeter, respectively. Communication with the picoammeter is via an RS-232 serial connection; communication with the electron gun power supply is via PCI cards.<sup>12</sup> We developed and implemented the algorithms to load the desired gun and picoammeter setting, pause for the necessary settling times, and record the signals for the SEY scans [48]. Development of the DAQP has been an important part of our SEY measurement program, resulting in a relatively sophisticated tool for control of SEY scans. The DAQP is identical for the 45° system, horizontal system, and off-line system.

## 4. Measurement Method: Phase I

Phase I measurements with the SEY stations in L3 began in January 2010 and ended when the stations were removed in January 2011. The techniques used for the Phase I measurements have been reported previously [21, 48, 49]. The SEY was measured on a 3 by 3 grid, as shown in Figure 3a. The energy was scanned from 20 eV to 1500 eV with a step of 10 eV.

In the Phase I algorithm, the program scanned through the energies and deflections with a constant sample bias, and the process was repeated after changing the bias.

The first scan was done with positive sample bias ( $V_b = 150$  V) to measure  $I_p$ , with gun settings for  $I_p \approx 2$  nA. This measurement was done with the deflection set to put the beam in a parking point between Point 5 and Point 9 of the grid (Figure 3a) to reduce conditioning at the measurement grid points.

The second scan stepped through the same gun energies with a negative bias ( $V_b = -20$  V) on the sample to measure  $I_t$ . At each gun energy, the beam was rastered across all 9 grid points while the program recorded the current for each point.

As indicated above, the gun output current varies with gun energy and drifts in time. To minimize the error due to the drift in gun current, we did a second  $I_p$  scan after the  $I_t$  scan. The first and second  $I_p$  values for a given energy were averaged for calculation of the SEY as a function of energy and grid point. Figure 6 shows examples of “before” (dotted lines) and “after” (solid lines) scans of  $I_p$ .

## 5. Measurement Method: Issues and Phase II Improvements

Our experience in Phase I led to iterations in the measurement method. Modifications for Phase II are described in this section. The modifications are outlined in Figure 7, along with the causal connections amongst them.

<sup>11</sup> Version 8.2, National Instruments, Austin, TX.

<sup>12</sup> PCI-6034E and PCI-6703, National Instruments, Austin, TX.



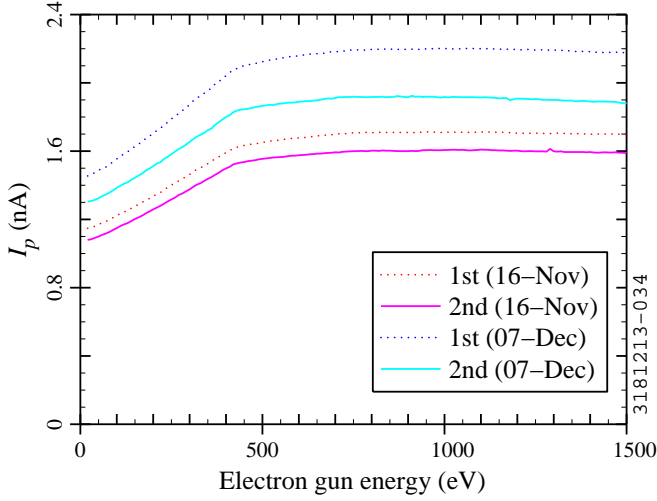


**Figure 6.** Repeated scans of primary current as a function of gun energy for the horizontal amorphous carbon sample (measured in 2010). The measurements labelled “1st” and “2nd” were done before and after an  $I_t$  scan (the  $I_t$  scan takes about 15 minutes). Ideally,  $I_p$  should be constant at 2 nA, but, in reality,  $I_p$  depends on the gun energy and varies from one scan to another.

The time line for the measurements and system modifications is outlined in Table 1. Significant improvements for Phase IIa were made between January 2011 and August 2011 when the SEY stations were out of the tunnel for hardware modifications, prior to the beginning of Phase IIa measurements; the hardware modifications are described in Sections 5.1, 5.4, and 5.6. Further improvements in the measurement methods were made between November 2011 and July 2012. The measurement hardware and techniques have been relatively stable since the start of Phase IIb in August 2012.

The changes for Phase II led to a significantly different timing algorithm for the SEY scans, shown diagrammatically in Figure 8; a zoomed-in version of Figure 8g is shown in Figure 9. For illustrative purposes, the horizontal axes in Figures 8 and 9 are not to scale and a simple  $n_x = 3$  by  $n_y = 3$  grid is shown ( $n_x$  and  $n_y$  are the number of horizontal and vertical grid points and  $n = n_x n_y$ ; see Appendix F for a version with a realistic number of grid points and a realistic time axis). Solid gray lines indicate a bias change; dashed gray lines indicate an increase in the gun current from the standby value to the full value; dotted gray lines indicate a deflection change. The final timing parameters used for Phase IIb are given in Table 2. Selected features of Figure 8 will be described in this section as the issues are discussed.

### 5.1. Ensuring Direct Photon Bombardment

With the closest bending magnet about 6 m from the samples, photons radiated by the electron beam in the bend are nearly tangent to the beam pipe wall (the angle is approximately 7 mrad from the tangent, though it varies by a small amount depending on the electron beam trajectory). As the sample diameter is approximately 16 mm, a sample which only slightly recessed from the beam pipe wall (by  $\geq 0.1$  mm) is masked by the pipe and does not receive any direct SR photons.

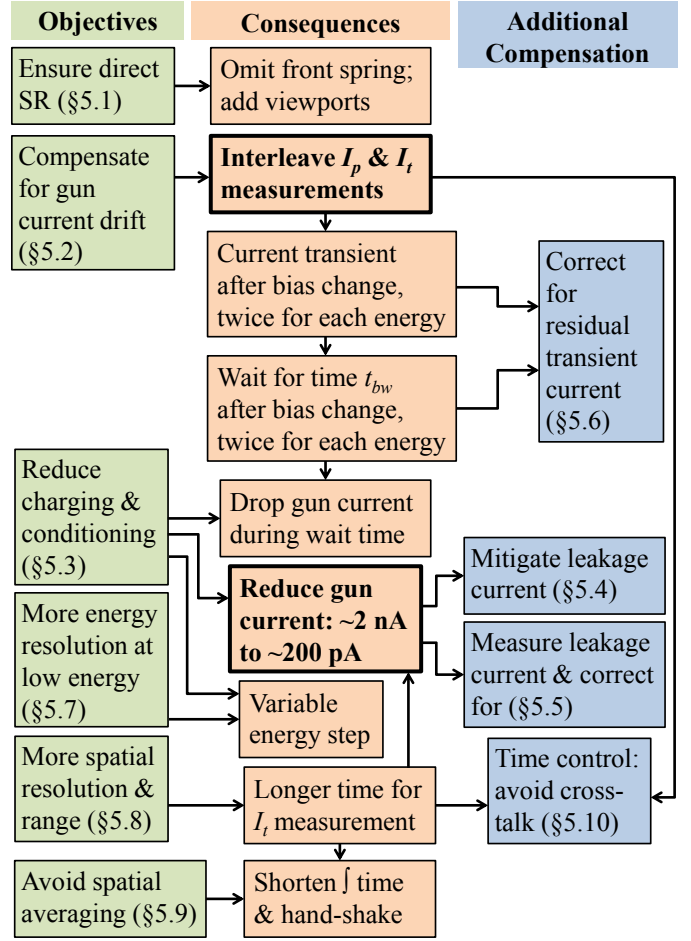


**Figure 7.** Flowchart showing the modifications to the SEY measurement method for Phase II and the interrelationships amongst various modifications. Changes with major ramifications are highlighted in bold type.

As shown in Figure 3, the sample design includes a groove in the front shoulder for a spring similar to that used in the back of the sample; the edge of the front spring is visible in Figure 3d. The front spring was used for the Phase I measurements. It is intended to ensure good electrical contact with the beam pipe so that the image currents of the passing bunches are minimally disrupted. Very little difference was observed in the SEY between the two samples in the Phase I measurements, which led to some doubt as to whether the samples might be slightly recessed from the beam pipe wall.

We replaced the beam pipe chamber after the end of Phase I due to a vacuum leak in the original chamber. We added viewports to the beam pipe opposite the samples to allow for inspection of the samples and verification of the sample position. Furthermore, we omitted the front spring in Phase II (as it is not required for typical CESR beam conditions, and, in fact, running beams with the samples out of the beam pipe is not a problem). We were able to confirm that the samples were slightly protruding into the beam pipe for all of the Phase II beam exposure periods. In Phase II, significant differences were observed in the early conditioning of the samples.

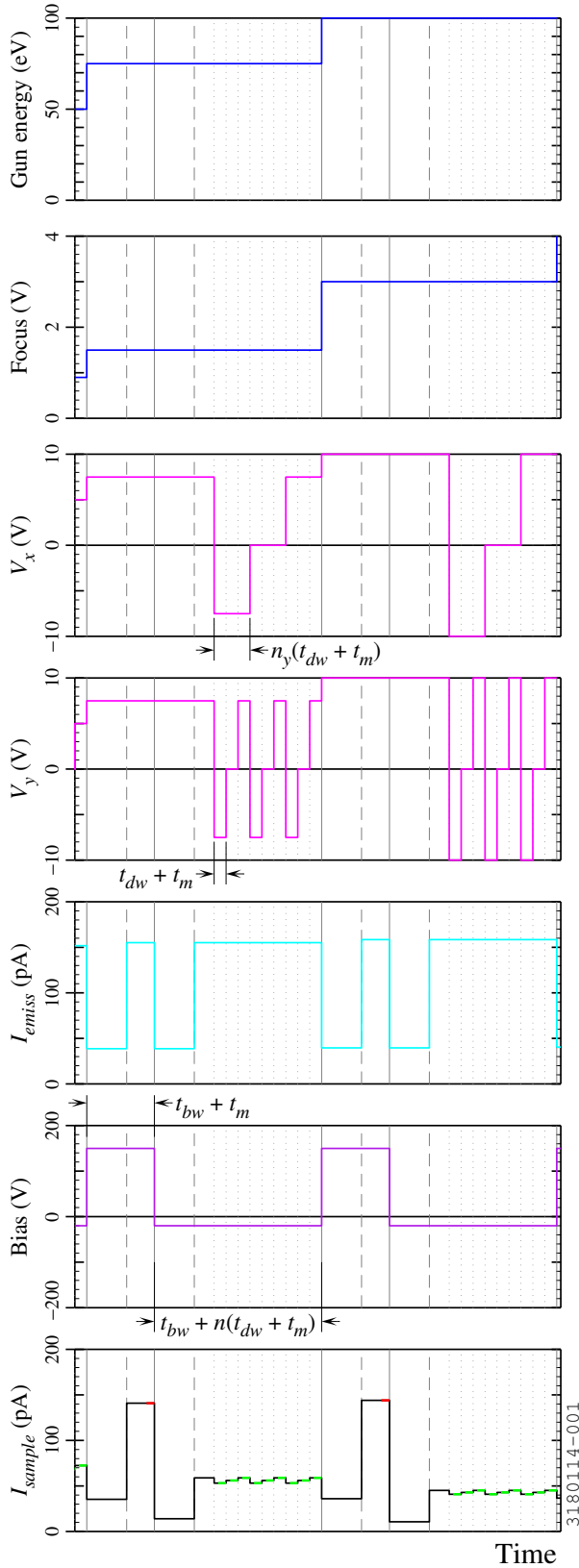


**Figure 8.** Timing schematic for SEY scans in Phase IIb: (a) gun energy, (b) focus, (c) horizontal deflection, (d) vertical deflection, (e) gun emission current, (f) sample bias, and (g) sample current as a function of time for 2 iterations (75 eV, 100 eV) in the energy scan. In (g), the averaging of  $I_p$  is in red and the averaging of  $I_t$  in green.

**Table 1.** SEY measurements in L3 and improvements in techniques.

Samples	Dates	Comments
<b>Phase I Measurements</b>		
TiN 1st pair	Jan 2010-Aug 2010	Commission systems
Al 6061-T6	Aug 2010-Nov 2010	Remove vacuum gauges
Amorphous C	Nov 2010-Jan 2011	
<b>Phase IIa Development</b>		
(Stations out of L3)	Jan 2011-Aug 2011	Ensure exposure to direct SR (§5.1); mitigate gun current drift (§5.2), charging (§5.3), & leakage current (§5.4–5.6)
<b>Phase IIa Measurements</b>		
Diamond-like C	Sep 2011-Nov 2011	Investigate spatial resolution
TiN 2nd pair	Nov 2011-Mar 2012	Improve spatial resolution (§5.9); variable energy step (§5.7); investigate spatial resolution & range
Cu OFHC	Mar 2012-Jul 2012	Improve spatial resolution & range
<b>Phase IIb Measurements</b>		
Stainless steel 316	Aug 2012-Sep 2012	Full spatial resolution & range (§5.8); mitigate parasitic conditioning (§5.3) & cross-talk (§5.10)
TiN 2nd pair	Oct 2012-Jan 2013	Recondition after exposure to air
Al 6063	Jan 2013-	

**Table 2.** Timing parameters for Phase IIb SEY scans.

Symbol	Value	Description
$t_m$	~ 250 ms	average and read out current
$t_{dw}$	50 ms	wait after setting gun deflection
$t_{cw}$	10 s	wait after setting gun current
$t_{bw}$	60 s	wait after setting bias

## 5.2. Mitigation of Electron Gun Current Drift

We observed in Phase I that the measured primary current ( $I_p$ ) changes slowly with time, in addition to being a function of energy. For the Phase I measurements on aluminum and amorphous carbon-coated samples, the “before  $I_t$ ” and “after  $I_t$ ” measurements of  $I_p$  differed by about 8% on average and by about 16% in the worst case. The first pair of measurements in Figure 6 are close to the typical reproducibility.

To reduce the systematic error due to current drift, a new measurement procedure was developed for Phase II in which  $I_p$

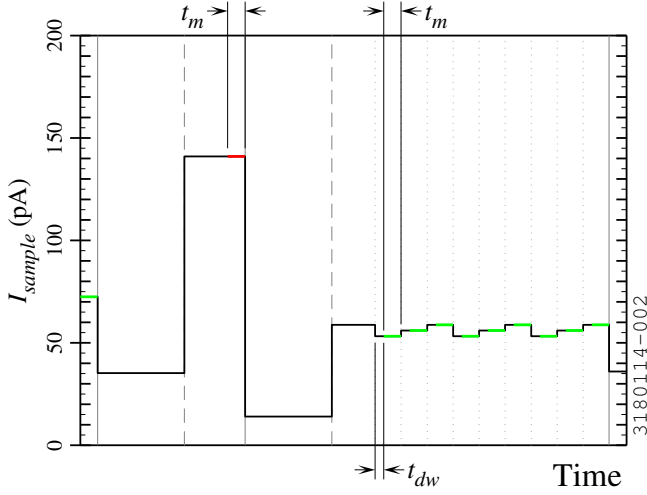


**Figure 9.** Zoomed-in timing schematic of sample current for SEY scans in Phase IIb. As in the previous figure, time intervals for averaging  $I_p$  are shown in red and time intervals for averaging  $I_t$  are shown in green.

measurements are interleaved with  $I_t$  measurements. As shown in Figure 8, the Phase II measurement sequence is to set the gun energy, apply a positive bias to the sample, move the beam to the parking point and wait for the current to stabilize, measure  $I_p$  at one grid point, apply a negative bias to the sample, park the beam and wait for the current to stabilize, measure  $I_t$  for all desired grid points, and then proceed to the next energy. As shown in Table 2, we wait for a time  $t_{bw} = 60$  s after changing the bias; this is a compromise between the need for a short measurement time and the need to allow the transient current to diminish (see Section 5.6 below). The longer waiting time required us to reduce the number of energy steps (Section 5.7).

With the Phase II method, we estimate that the error in the current measurements due to gun current drift is  $\lesssim 2\%$ .

### 5.3. Reduction of Charging and Parasitic Conditioning

SEY measurements on samples with diamond-like carbon (DLC) coatings on aluminum were first done in 2011 in the off-line SEY station. The DLC coatings are being evaluated by KEK for SEY reduction and EC mitigation. Our DLC samples were provided by S. Kato (KEK). A measurement on DLC using the Phase I method is shown in Figure 10 (blue circles). The SEY curve appears distorted. We suspected that the distortion was due to charging of the DLC-coated surface by the electron beam. The charging is presumably due to the DLC coating having insulator-like properties. Qualitatively similar effects have been reported in SEY measurements on other materials (for example, measurements on MgO by Scholtz *et al.* [52]).

To test the charging hypothesis, we remeasured the SEY with a long wait time (3 to 4 minutes) between each energy step to allow the surface to discharge, and with a smaller electron gun current ( $\sim 0.5$  nA instead of  $\sim 2$  nA) to reduce the supply of charge to the sample. To avoid charging during the waiting period, a single grid point was measured, and the electron beam was parked at a different grid point during the waiting period. The results are shown in Figure 10 (red squares). As

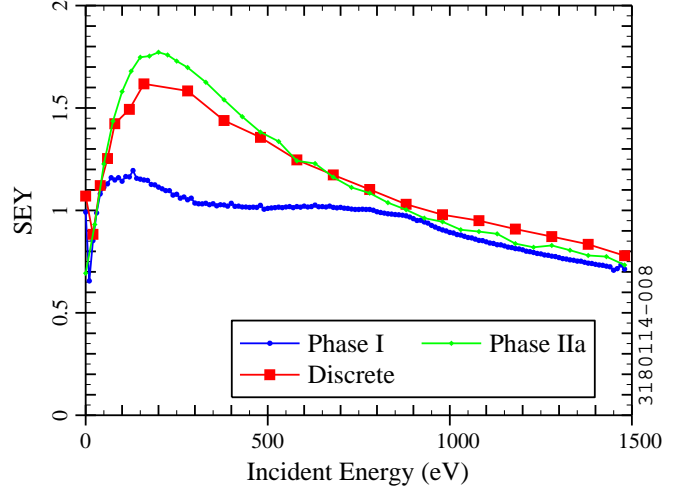


**Figure 10.** SEY as a function of incident electron energy for a diamond-like carbon-coated aluminum sample, comparing different measurement methods. The middle grid point is shown ( $\theta = 25^\circ$ ). Blue: Phase I method ( $I_p \sim 2$  nA, 5 seconds for each energy, 9 grid points measured). Red: “discrete” scan (large energy step,  $I_p \sim 0.5$  nA, 3 to 4 minutes waiting period with the electron beam parked away from the middle point before each measurement; only 1 grid point measured). Green: Phase IIa method ( $I_p < 0.2$  nA, 9 grid points, beam parking away from middle grid point).

can be seen, the additional delay with the beam deflected and the reduction in current produced a significant increase in the measured SEY. The new curve is closer to what one would expect based on measurements of other materials, as well as being more consistent with other measurements on DLC [31, 33, 39].

The results on DLC motivated us to reduce the electron gun current for measurements in L3. In Phase II, we used  $I_p \sim 0.2$  nA for standard measurements. A side benefit of the current reduction was to reduce unintended conditioning of the sample by the electron gun, which, as discussed in Section 3.3, should be minimised in order to accurately measure the effect of the accelerator environment. A complication is that, in Phase II, we switched the bias to measure  $I_p$  and  $I_t$  at each energy (Section 5.2), with a longer waiting time to mitigate the transient current (see Section 5.6 below). The longer waiting time increased the integrated current per energy step; to shorten the measurement time and reduce charging and conditioning, we adjusted the number of energies measured (see Section 5.7 below). The net result was an increase in the integrated flux for the parking point and a decrease in integrated flux for other grid points. A measurement on the same DLC sample (in the  $45^\circ$  station) using the Phase IIa method is also included in Figure 10 (green diamonds). The differences between the discrete scan and the Phase IIa scan are mainly due to the leakage correction (see Sections 5.5 and 6.3) included in the Phase IIa case.

In Phase I, the parking point was between two grid points (Section 4). In Phase II, due to the smaller deflection step, the parking point was also a measurement point, as shown in Figure 12b below. Hence, in Phase II, we measured the SEY at the parking point, though there were issues with spatial resolution in Phase IIa (see Section 5.9).

In Phase IIb, an additional improvement was introduced,



which was to decrease the electron gun current by about a factor of 4 while waiting for the sample current to stabilize after a change in the bias. The gun current is lowered for 50 s and then we return to the nominal gun parameters for a time  $t_{cw} = 10$  s to allow the gun emission current to stabilise before the measurement (Figure 8). The current modulation reduces the dose to the parking point by about a factor of 3.5. Details on how the current modulation was implemented can be found in Section A.2. Though different in the details, our method of current modulation is conceptually similar to previously-used techniques for insulating materials (see [52], for example).

With current modulation and Phase IIb parameters, one SEY scan produces an integrated electron flux of  $\sim 0.8 \mu\text{C}/\text{mm}^2$  for the parking point and  $\lesssim 12 \text{ nC}/\text{mm}^2$  for the other grid points. In past studies on electron gun conditioning by other groups, the peak SEY decreased by  $\lesssim 10\%$  for doses of order  $1 \mu\text{C}/\text{mm}^2$  for Cu [27, 29], TiN [41], and Al [42]. Based on this, we would expect to see a small amount of conditioning at the parking point on unconditioned samples. (However, there may be less conditioning in our Phase II SEY scans because the electron energy is low for a large fraction of the scan, and it has been found that conditioning is less efficient at low energies [53]).

We did not see a significant difference in the parking point's SEY for Cu, stainless steel, TiN, or Al in Phase II. An example is shown in Section 7.

As described above, we found DLC to be more susceptible to charging. Off-line measurements on an unconditioned DLC sample with Phase IIb parameters showed a decrease in the measured SEY at the parking point with current modulation ( $\sim 7\%$ ) and a larger decrease without current modulation ( $\sim 24\%$ ). On the other hand, a conditioned and air-exposed DLC sample did not show a difference in measured SEY at the parking point. Additional measurements on DLC and amorphous C are being done in the off-line station to better quantify their susceptibility to charging and conditioning and check the reproducibility of our observations.

#### 5.4. Leakage Current: Mitigation

Ideally, the picoammeter measures only the current due to primary and secondary electrons. In reality, because the insulators are imperfect, additional current flows through the picoammeter to ground when the voltage bias is applied; this is generally referred to as “leakage current.” As has been pointed out previously, the leakage current should be a small fraction of  $I_p$  to avoid systematic errors in the calculated SEY [43]. In Phase I, no leakage corrections were applied. As discussed in the preceding section, initial measurements on DLC led us to reduce the electron gun current in Phase II. Because the relative contribution from the leakage current increases as the gun current decreases, an effort was made to quantify the leakage current and ascertain its effect while preparing for Phase II.

Measurements indicated that the leakage current was strongly correlated with the ambient humidity. At high humidity, we found that the leakage could be as high as several nA (hence exceeding  $I_p$ ) and could vary significantly in the time needed for an SEY scan, which could produce large errors in the measurements.

As discussed in Section 3.6, we use a small shielded circuit to apply the bias to the triaxial cable. We found that there was significant leakage in one of these circuits. The circuits were re-soldered more carefully and the exposed conductors were painted with a silicone coating<sup>13</sup> to provide a moisture barrier. After this modification, the main leakage paths were found to be the insulating stand-offs and the ceramic break (shown in green in Figure 5).

The decrease in resistivity of insulators due to moisture has been extensively documented in the literature in the past century (see, for example, Refs. [54–56]). In a humid environment, current is conducted along the surface of an insulator, where there is a layer of moisture from the ambient air. These considerations led us to a redesign: (i) the original G10 stand-offs were replaced by similar parts with a smoother surface finish, more careful cleaning, and with blind holes instead of through holes; (ii) a nitrogen gas “blanket” was made to isolate the ceramic break from the ambient air. The blanket was established by covering the ceramic with a Teflon tube made from 2 halves. As shown in Figure 11, the tube is attached to the grounded flange of the ceramic break, with a small gap on the biased flange of the ceramic break to avoid adding another path for the leakage current. (In Figure 5, the Teflon tube is blue and the blanket region and gap are orange.) The presence of the gap required us to use a steady flow of nitrogen gas (about 2.5 SCFH  $\approx 20$  mL/s per station) to establish the blanket. The  $\text{N}_2$  gas source is boil-off from the building's liquid nitrogen storage Dewar, hence it has very low moisture content.

With high humidity, the nitrogen blanket alone did not produce a low and stable leakage current; we had to first warm

<sup>13</sup>Silicone Conformal Coating, 422-55ML, MG Chemicals, Surrey, BC, Canada.

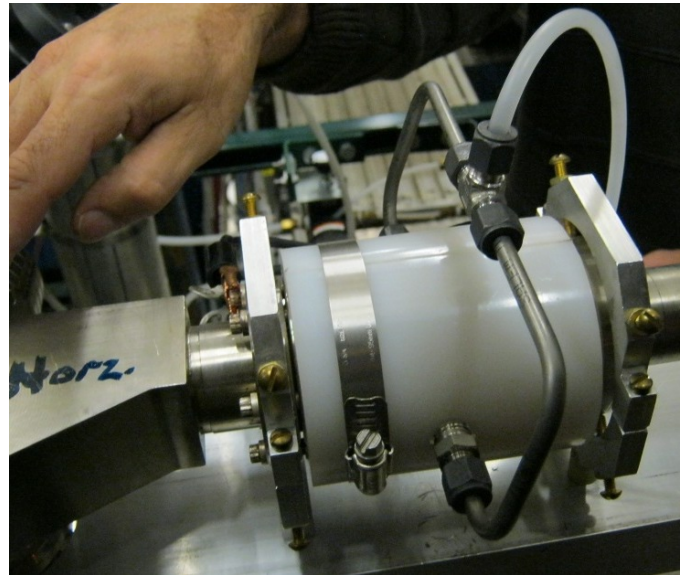


**Figure 11.** Photograph of the horizontal SEY station after installation of a two-piece Teflon tube to establish a nitrogen gas blanket around the ceramic break. The tube is connected to the grounded SEY chamber on the left. There is a small gap on the right between the tube and the biased sample positioner arm.

the ceramic with a heat gun to remove the existing moisture. We found that even a brief interruption in the gas flow allowed moisture to return, necessitating a reheat of the ceramic. In a dry environment, the leakage current with gas flow was stable without the need to heat the ceramic. At a low relative humidity, the leakage currents with and without gas flow were comparable. Additional information on the correlation between humidity and leakage current can be found in [Section E.1](#).

After the modifications to the system, the typical leakage current was of order 30 pA or less at  $V_b = 150$  V. This corresponds to an error of  $\lesssim 14\%$  in the  $I_p$  measurement for Phase II parameters (not including the transient contribution, which is discussed in [Section 5.6](#)). Repeated measurements indicated that the leakage current could still vary over time, even with the gas blanket. The variation can be as much as a factor of 2 over long periods, as discussed in more detail in [Section E.2](#).

### 5.5. Leakage Current: Measurement

As discussed above, even with mitigation, the leakage current is not negligible relative to the Phase II gun current. Consequently, in Phase II, we added the step of measuring the leakage current prior to each SEY measurement. The leakage scan is done with the same data acquisition method as the SEY scan, but with the electron gun turned off. We found that it is better to repeat several iterations of positive and negative sample bias to allow the current to stabilise; however, we perform fewer iterations for the leakage scan (16 typically) than for the SEY scan (44 typically).

As will be discussed in [Section 6.3](#), the measured values of  $I_p$  and  $I_t$  are corrected by subtracting the measured leakage current with the corresponding sample bias before calculating SEY. [Section E.2](#) includes more information on the measured leakage as a function of time over the course of Phase II.

Time permitting, a second leakage scan is done after the SEY scan to quantify the leakage current stability. Typically, the leakage currents before and after the SEY measurement agree within  $\pm 2$  pA with positive bias ( $V_b = +150$  V) and within  $\pm 0.5$  pA with negative bias ( $V_b = -20$  V). Hence we estimate that the leakage current drift contributes an error in the measured and corrected currents of about 1% of  $I_p$  for the Phase II parameters.

### 5.6. Transient Current: Mitigation

A change in the sample bias produces a transient in the sample current due to the stray capacitance of the system and the response of the picoammeter. The stray capacitance includes a contribution from the triaxial cable and the SEY station, whose biased positioner arm is in proximity to the grounded tube leading to the beam pipe and the grounded support beam ([Figure 5](#)). In the initial measurements, the SEY stations made use of a special kapton-insulated gasket instead of the ceramic break, and included bellows intended to ease the alignment of the sample positioner with the beam pipe hole. Drawings showing the original design can be found in an earlier paper [48]. Prior to the start of Phase II, the insulated gasket and bellows were replaced with a traditional gasket and ceramic break (as shown in

[Figures 1, 2, and 5](#)). We estimate that the change from the insulated gasket to the ceramic reduced the capacitance to ground from 1.4 nF to 10 pF.

After these hardware modifications, the transient signal was nevertheless large, with a current spike peaking at about 0.5 nA (hence exceeding the nominal  $I_p$  for Phase II), and a decay time of order 30 s (examples are included in [Appendix D](#)). Ideally, one would wait for the current to reach its equilibrium value before starting the measurement. In Phase I SEY scans, the bias voltage was switched only twice, so an extended waiting period after a bias change was tolerable. A wait time of several minutes was found to be adequate.

On the other hand, with the Phase II procedure to mitigate the gun current drift ([Section 5.2](#)), the bias is switched twice for each energy ([Figure 8f](#)), making a long wait time after each bias change impractical, given the time available for the weekly tunnel access. Though the capacitance reduction associated with the station redesign helped, the time to reach equilibrium was still too long for practical measurements. Hence a compromise solution was necessary: waiting for time  $t_{bw} = 60$  s after a bias change, reducing the number of energy steps ([Section 5.7](#)), and correcting for the residual effects from the transients. Because the leakage scans described above are done after switching the bias with the same timing algorithm as is used for the SEY scans, the leakage measurement also includes a contribution from the transient current that has not vanished completely in the 1 minute wait time. The correction for the leakage current thus also corrects for the residual transient current, which is about 4% of  $I_p$  for the Phase II parameters.

Initial leakage measurements were done in conjunction with SEY scans on 9 grid points. Because of the relatively short time required for the  $I_t$  measurements, the leakage scans were done using only 1 grid point. When the number of grid points was increased for improved spatial resolution (see [Section 5.8](#) below), we began using the same number of grid points for the leakage scan as for the SEY scan. The transient response of the system produces a change in the measured leakage current over the time required to measure all of the grid points (see [Figure 15](#) below). When recording the current, we also recorded the time stamp (with 0.1 ms resolution) in order to know the time elapsed since the most recent change in sample bias, which varies from one energy iteration to another for a given grid point due to the variation in the number of grid points for higher energies ([Section 5.8](#)) and the adjustments to the waiting time ([Section 5.10](#)). A time dependence was included in the leakage correction to account for the change in current during the  $I_t$  measurements, as will be described in [Section 6.3](#).

### 5.7. Energy Resolution and Segmentation

As indicated above, Phase I measurements were done with a starting electron gun energy of 20 eV, a final energy of 1500 eV, and an energy step of 10 eV. Because low-energy electrons are thought to be important to the build-up of the electron cloud, a variable energy step was introduced in Phase II to allow for smaller steps at lower energies in routine measurements. At the same time, the procedure was adjusted so that both  $I_p$  and  $I_t$  were measured in a single energy scan ([Section 5.2](#)), with

long waiting times at each energy (Section 5.6). To keep the overall measurement time short enough to be compatible with the weekly access schedule, the energy step was increased for higher energies (we were also motivated by the need to minimise charging and conditioning by the electron beam, as discussed in Section 5.3). This resulted in a net decrease in the number of energies measured. The energy segments for the variable-step scans are given in Section B.1.

### 5.8. Improved Spatial Resolution and Range

As discussed above, the Phase I measurements were done over a 3 by 3 grid (Figure 3a). We found that more detailed information would be useful to give us a more complete picture of the SEY's dependence on position and angle. Consequently, we implemented scans with increased range and resolution in Phase II. A uniformly-spaced grid with high resolution and full range was not practical for weekly measurements, so a compromise solution was developed: scanning with high resolution and full range, but only over 3 horizontal segments and 3 vertical segments. (Occasional “high definition” scans are done with high resolution and full range over the entire sample when additional time is available.) The grid points are shown in Figure 12. The corresponding deflection parameters are listed in Section B.3. One complication is that the largest deflections cannot be reached at high energies, because the voltages that can be applied to the electron gun deflecting electrodes are limited to  $\pm 150$  V. The colors in Figure 12 indicate the maximum gun energy measured for each grid point. The data acquisition software begins to skip some grid points when the gun energy exceeds 600 eV, and measures only about half of the grid points at the highest energy. This complicates the timing of the measurements, as will be discussed in Section 5.10.

For simplicity, the grid point layout shown in Figure 12 is measured using two arrays of electron gun deflections. As a result, 9 of the grid points are measured twice (the repeated points coincide with the points in the 3 by 3 grid of the Phase I measurements). This provides some additional information about systematic and statistical errors. In Phase IIa, the data acquisition software allowed only one array, which required us to run the SEY measurement twice. In Phase IIb, we implemented the option of specifying 2 arrays of gun deflections, so that all of the grid points could be measured in one energy scan. This allowed us to shorten the measurement time significantly, since the majority of the time is spent waiting for transients to settle after changing the sample bias.

To avoid additional complications in the data acquisition algorithms, the electron gun deflection is varied linearly from one grid point to the next, leading to the uniformly spaced deflection angles shown in Figure 12a (strictly speaking, it is the tangent of the deflection angle that has a constant increment). Because the electron gun axis is at  $25^\circ$  relative to the sample axis, the grid point spacing is not exactly symmetric between the left and right sides of the sample. Moreover, the sample face is curved, which produces some distortion in the grid spacing between the middle of the sample and the upper and lower portions. These asymmetries in the grid layout can be seen in Figure 12b. In the analysis of the SEY measurements, the curvature of the sample

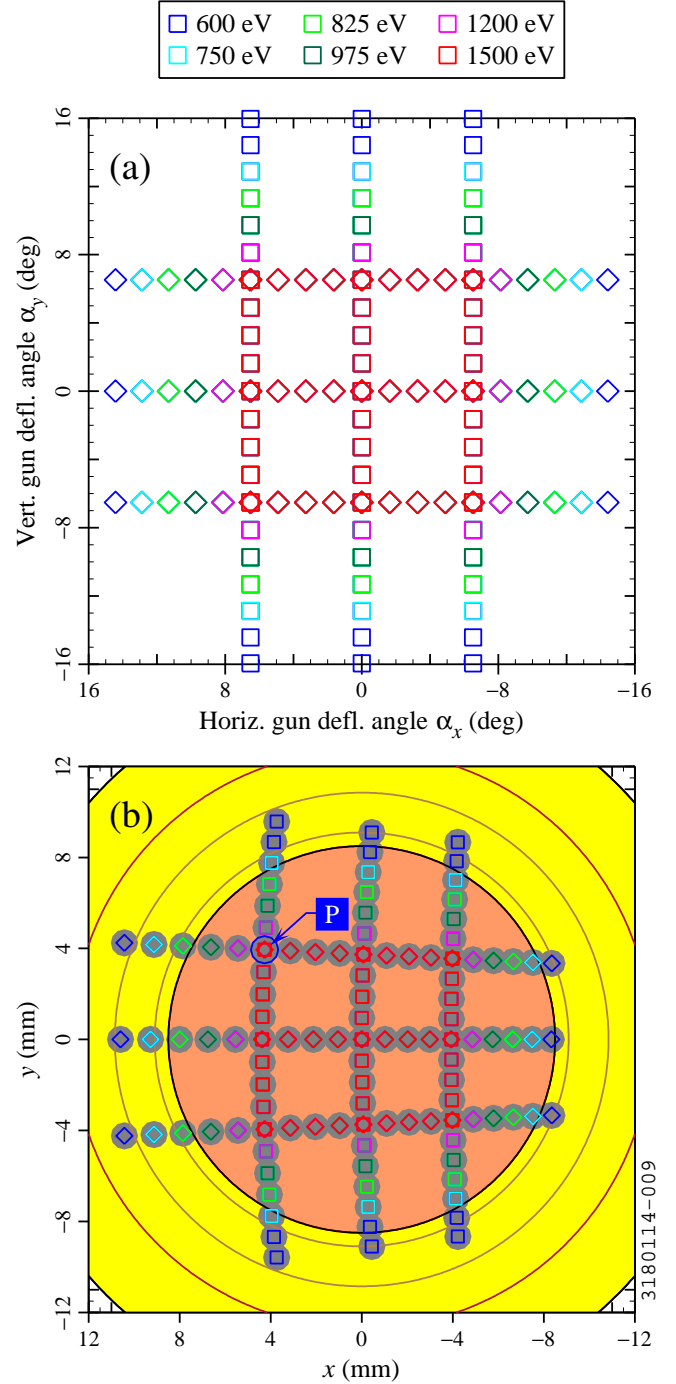


**Figure 12.** Grid points for double scans. (a) Gun deflection angles for each grid point. (b) Sample coordinates for each grid point ( $x$  and  $y$  are the horizontal and vertical distance from the middle of the sample, respectively, in Cartesian coordinates). Legend: maximum gun energy measured for each grid point. Squares: first array; diamonds: second array. Solid gray circles: estimated beam spot size at high gun energy. Orange: sample face; yellow: sample shoulder. Brown circles: edges of groove for the front spring and outer shoulder edge. P: parking point.



and the angular offset of the gun are taken into account when calculating grid point coordinates.

In [Figure 12b](#), the sample's face is shown in orange and the sample's shoulder is shown in yellow. The brown circles represent various features on the shoulder (which can be seen more clearly in [Figure 3](#)). As can be seen, the grid point coordinates are not all on the sample face.<sup>14</sup> The solid gray circles indicate the estimated beam size for a gun energy of 1500 eV (not taking into account possible distortion in the size and shape of the beam spot for large deflecting angles). There is some overlap between adjacent grid points over the majority of the sample. As discussed in [Section 3.5](#), the estimated beam spot size is smaller at intermediate energies; for the smaller spot size, none of the grid points overlap.

The horizontal axes in [Figure 12](#) are reversed in order to show the grid points as viewed by an observer looking at the front of the sample (the  $xy$  coordinate system being based on the sign convention for the electron gun deflection electrodes).

### 5.9. Spatial Resolution: Time Control and Hand-Shaking

In the Phase I measurements, there was no “hand-shaking” operation between the DAQP and picoammeter. We unintentionally used incompatible timing parameters between the picoammeter and the DAQP: the picoammeter was set up to average the current over 1 second, but the DAQP waited for only 0.2 s after a change in the deflection. As a result,  $I_t$  measurements for grid points other than the first point included significant averaging over more than one grid point. The DAQP used a waiting time of 1.5 s after an energy step, so there was no unintentional mixing of different energies.

After measurements on the first few samples, the timing of the current measurements was investigated more closely. We realised that the picoammeter and DAQP timing parameters were indeed incompatible. (Nevertheless, a statistically significant variation in SEY as a function of grid point was observed in the early measurements [48, 49], in spite of the unintended averaging over multiple grid points.)

After this problem was identified, alternative timing methods were investigated. We found that we could decrease the averaging time without making the noise-to-signal ratio excessively large. A hand-shaking algorithm was ultimately chosen: after adjusting the energy, bias, and deflection, the DAQP waits for a settling time  $t_{dw}$ , and then instructs the picoammeter to clear its buffer, average the current, and return the averaged value. The DAQP waits for the picoammeter's value before proceeding to the next deflection (or next combination of deflection, bias, and energy). Because the deflection is set prior to the start of the picoammeter's measurement, the value does not include contributions from previous grid points. With the new method, the current is averaged over  $\frac{1}{6}$  sec. Including the time for communication with the picoammeter and the wait time after setting the deflection ( $t_{dw}$ ), the net measurement time per

grid point is about 0.3 sec. Additional information about the picoammeter parameters is given in [Section A.3](#).

### 5.10. Time Control: Cross-Talk Avoidance

As discussed in [Section 3.6](#), low-noise triaxial cables connect the sample positioner arms to the picoammeters, but the positioner arms are not electrically shielded. In L3, the stations are relatively close to one another (when they are in the beam pipe, the samples are about 0.4 m apart). As shown in [Figure 8f](#), the Phase II SEY scan algorithm requires two steps in the bias voltage for each energy. We observed that a change in bias on one sample produces a spike in the measured current of the other sample. With Phase II parameters, the current perturbation can be up to about 50% of  $I_p$ . However, the current spikes due to cross-talk have a short duration ( $\lesssim 0.2$  sec), in contrast to the current transients due to a bias change, which require a long waiting time.

If the bias of one sample is changed while the current of the other sample is being measured, this can produce a noise spike in the measured SEY. To illustrate, [Figure 13a](#) shows repeated SEY measurements done on copper in the 45° system during Phase IIa with 63 grid points. A large spike in SEY is present for 1 out of 4 measurements. The spike appears at different energies for different grid points (a single grid point is shown in [Figure 13a](#)), though always for  $K \gtrsim 1000$  eV. In this case, the upward spikes in SEY are the result of downward spikes in  $I_t$ . No spikes are seen for the horizontal sample.<sup>15</sup>

[Figure 13b](#) shows the delay between current measurement times for the two systems. The delay values are based on the time stamps for the  $I_p$  measurements. The shaded areas indicate “quiet zones”: if the time delay overlaps a shaded area, there is a risk of a spike in the recorded current due to a bias change by the other system. For the present example with 63 grid points, the red and orange areas are the relevant ones. The spikes are observed when the delay is in an orange zone (blue curve,  $K \gtrsim 750$  eV). This is consistent with our hypothesis that the spikes are due to cross-talk between the systems.

To avoid the cross-talk, we implemented a delay between the start times for the scans on the 2 samples to ensure that we did not switch the bias for one system when measuring the current on the other system. With a waiting time after a bias change of  $t_{bw} = 60$  s, there is a timing margin of about  $\pm 30$  s for measurements on one grid point (indicated by the red zones in [Figure 13b](#)). With the 120 grid points used for Phase IIb scans with improved range and resolution, the  $I_t$  measurements take about 35 s, which reduces the timing margin to about  $\pm 12$  s (yellow zones in [Figure 13b](#)). The basis for this timing margin is discussed in [Appendix F](#), which includes an example of current measurements during a simultaneous SEY scan with both stations.

Even with control of the start time delay, spikes still occurred for a significant fraction of the SEY scans. Further investigation indicated that occasionally the time to measure one

<sup>14</sup>For simplicity, [Figure 12b](#) does not show the actual point of impact for grid points that are not on the sample's face—when the beam does not hit the face, it travels a longer distance, resulting in additional transverse motion.

<sup>15</sup>For simplicity, the incident energy in [Figure 13](#) is not corrected to account for the gun deflection (see [Section 6.1](#)).

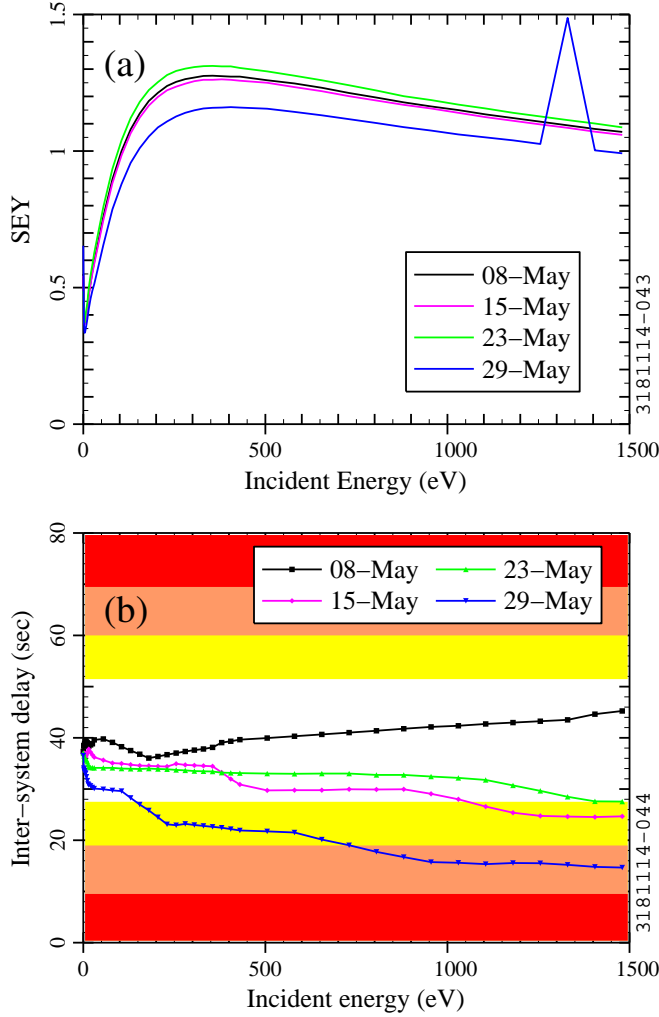


**Figure 13.** Examples of SEY scans without timing compensation using 63 grid points (Cu, May 2012): (a) SEY as a function of incident energy for 45° sample ( $V_x/V_{gsp} = -0.1$ ,  $V_y/V_{gsp} = +0.05$ ). (b) Timing delay of 45° system relative to horizontal system. Shaded areas: “quiet zones” for current measurements with 1 grid point (red), 63 grid points (orange), and 120 grid points (yellow).

grid point is significantly longer than the nominal 0.3 s, sometimes being  $\sim 1$  s. When the longer delays are random, there is little cumulative effect. With the large number of grid points used in Phase II, we found that a cluster of several longer delays sometimes occurs for one system, accumulating enough time difference to produce cross-talk again. The problem can be seen in Figure 13b: the delay between the two systems is initially about the same for all 4 scans, but it varies during the scan, with 3 out of 4 cases getting near to or crossing into a yellow area, and hence being marginal or unsuitable for scans with 120 grid points.

We suspected that hand-shaking (Section 5.9) was a source of time variation. However, we found that the hand-shake wait time (time spent by the DAQP waiting for the picoammeter to return a value) varies by only a few ms. The evidence suggests that the time to write values to the data file is the main cause for the occasional long delays (at present the DAQP write the current to the data file after each grid point, and generally the

file is on a remote file system for logistical reasons).

To eliminate the cross-talk problem in a reliable way, we modified the timing algorithm. When we initiate a measurement, the data acquisition program uses the wait times and expected measurement time per point to predict the overall time per energy step. After each energy step, the DAQP checks the time elapsed. In the next energy step, it adjusts the wait time before the  $I_p$  measurement ( $t_{bw}$  with  $V_b = -150$  V) to compensate for the actual time of the previous step being different from the desired time. This prevents the timing variations from producing a large cumulative time offset. It has the side effect that the wait time varies from one energy to another; this is taken into account in the data analysis, as discussed in Section 6.3.

Figure 14 shows some examples of SEY scan timing with compensation. There is little cumulative change in the delay between the two systems, and there is a comfortable timing margin for scans with 120 grid points. We did not observe any spikes in the SEY due to cross-talk after implementing the compensation algorithm.

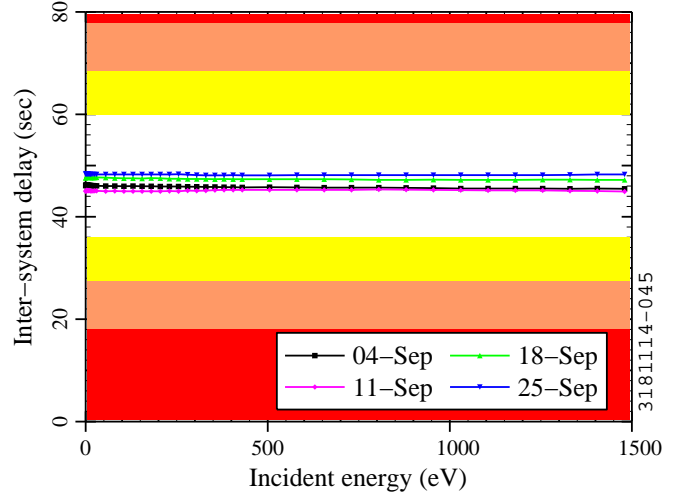


**Figure 14.** Examples of inter-system timing delay with timing compensation using 120 grid points (stainless steel, September 2012). Shaded areas: “quiet zones” for current measurements with 1 grid point (red), 63 grid points (orange), and 120 grid points (yellow).

For scans with increased spatial range, there is the additional complication that the number of grid points decreases with energy for gun energies above 600 eV, as discussed in Section 5.8. The DAQP accounts for this by subtracting the number of skipped grid points when calculating the expected time for a given iteration. As a result, the nominal wait times are the same for all energies. As long as their start times have the appropriate offset, the 2 systems remain synchronised as the time per iteration decreases.

### 5.11. Final Measurement Procedure

Our procedure for SEY measurements in Phase IIb is as follows: (i) move the samples from the beam pipe to the measurement position and close the gate valves; (ii) do a leakage scan, switching between positive and negative bias (Section 5.5); (iii)

warm up the electron guns for 30 to 60 minutes and then adjust the gun parameters to make  $I_p$  approximately 200 pA (Section 3.4); (iv) do an SEY scan; (v) repeat the leakage scan if time permits; (vi) return the samples to the beam pipe. With our standard parameters, the leakage scan takes 40 minutes and the SEY scan takes 110 minutes. Including set up and removal of the equipment, the full measurement takes about 5 hours. This requires us to measure the samples in parallel rather than sequentially, since the access time is typically 6 hours or less.

## 6. Data Analysis

The SEY is calculated from  $I_p$  and  $I_t$  using Equation (2). The gun energy is corrected to account for the effect of the electrostatic deflection. The sample's voltage bias is taken into account when associating the SEY with an incident energy. The measured values of  $I_p$  and  $I_t$  are corrected to account for leakage current and current transients when calculating the SEY.

### 6.1. Energy Correction for Electrostatic Deflection

The electron gun accelerates its electrons to the set point energy with a longitudinal electrostatic field. Paired deflection plates at the exit of the gun deflect the electrons electrostatically to the desired horizontal angle ( $\alpha_x$ ) and vertical angle ( $\alpha_y$ ) relative to the axis of the gun. Because the kicks are produced by an electric field, they change the kinetic energy of the electrons, in addition to changing their direction. Hence the kinetic energy  $K_g$  of the electrons is larger than the set point value  $K_{gsp}$  when they are deflected. In the non-relativistic case,

$$K_g = K_{gsp}[1 + \tan^2(\alpha_x) + \tan^2(\alpha_y)] \quad (3)$$

For the 3 by 3 grid used in Phase I, the gun energy is 2.6% higher than the set point energy in the worst case. For the standard double grid used in Phase IIb, the gun energy increases by 9.5% in the worst case. The energy correction was not included in the preliminary reports on the SEY measurements [21, 48–50], though most of the results were for the middle of the sample, where no correction is needed.

### 6.2. Correction for Sample Bias Voltage

The SEY is in general a function of the kinetic energy  $K$  and angle  $\theta$  of the incident primary electron:  $\text{SEY} = \text{SEY}(K, \theta)$ . The measurements of  $I_p$  and  $I_t$  are done while scanning the gun energy (as indicated in Table 5). Because the sample is biased, the incident kinetic energy of electrons reaching the sample is the sum of the electron gun energy ( $K_g$ ) and the electron charge magnitude ( $q_e$ ) times the bias voltage ( $V_b$ ):

$$K = K_g + q_e V_b \quad (4)$$

As a result, the incident energy is in principle smaller than the gun energy by 20 eV when we measure  $I_t$  with  $V_b = -20$  V and larger by 150 eV when we measure  $I_p$  with  $V_b = 150$  V. Ideally, the negative bias for the  $I_t$  measurement repels all of the secondary electrons produced at the surface of the sample, while the positive bias prevents the escape of any secondaries. With

the assumption that the intrinsic primary current to the sample is independent of the bias voltage and that no secondaries escape with  $V_b = 150$  V for the  $I_p$  measurement, we may use  $V_b = -20$  V in Equation (4) to calculate the appropriate incident energy  $K$  associated with the measured SEY. This correction is included for recent measurements [50], though we plotted SEY simply as a function of  $K_g$  for early analyses [21, 48, 49].

Because the primary electrons' incident angle is not normal to the sample ( $\theta \neq 0$ ), the sample bias can change not only the kinetic energy of the incident electrons, but also their trajectory, and hence can shift their incident angle and impact position before the electrons reach the sample. A simple analytic model suggests that this effect will be significant for electron energies of order 100 eV and lower (at 100 eV, the model predicts a shift in the incident angle of  $3^\circ$  and a shift in the impact point by 1 mm for the middle grid point). The analytic model assumes a simplified electric field and is likely to overestimate the deflection. At present, our data analysis does not account for the shift in angle and impact position (we plan to develop a model that describes the SEY measurements in a more complete way in the future). As a result, the reader should be cautious about making inferences about the SEY for energies lower than about 100 eV based on our measurements.

### 6.3. Time-Dependent Correction of Leakage Current and Current Transients

In Phase I,  $I_p$  was about 2 nA; in Phase II, we decreased  $I_p$  to about 200 pA to reduce charging and conditioning (Section 5.3). As a result, the leakage current became a larger fraction of  $I_p$ , and we took steps in Phase IIa to mitigate (Section 5.4), measure (Section 5.5), and correct for the leakage current. A static leakage correction was done initially: the leakage current was measured with the same bias voltages as for the SEY measurement and the average leakage current for each bias was subtracted from  $I_p$  and  $I_t$ . In the leakage measurement, the bias was switched with the same wait time as for the  $I_p$  and  $I_t$  measurements, in order to account for the transient response of the system (Section 5.6).

In the course of Phase IIa, we increased the number of grid points for better spatial resolution (Section 5.8), and began to measure the leakage current with the same timing of bias switching as done for the SEY measurement; we observed that the leakage current was changing slowly in the time required to measure all of the grid points. This led us to develop a model for the leakage current that includes a contribution from the transient current. The derivation of the model is given in Appendix D. We use the time-dependent leakage model for the analysis of Phase II measurements with more than 9 grid points.

Figure 15 shows an example of leakage scans on both stations. The lightly-colored markers (magenta and cyan) indicate the measured (“raw”) current as a function of time. With  $V_b = 150$  V (Figure 15a), the leakage current is about 20 pA for the horizontal station and about 30 pA for the  $45^\circ$  station. With  $V_b = -20$  V (Figure 15b), the leakage current is about  $-8$  pA for the horizontal station and about  $-5$  pA for the  $45^\circ$  station. The measurements with negative bias are repeated 120 times, which takes about 35 s, following the same timing algorithm as



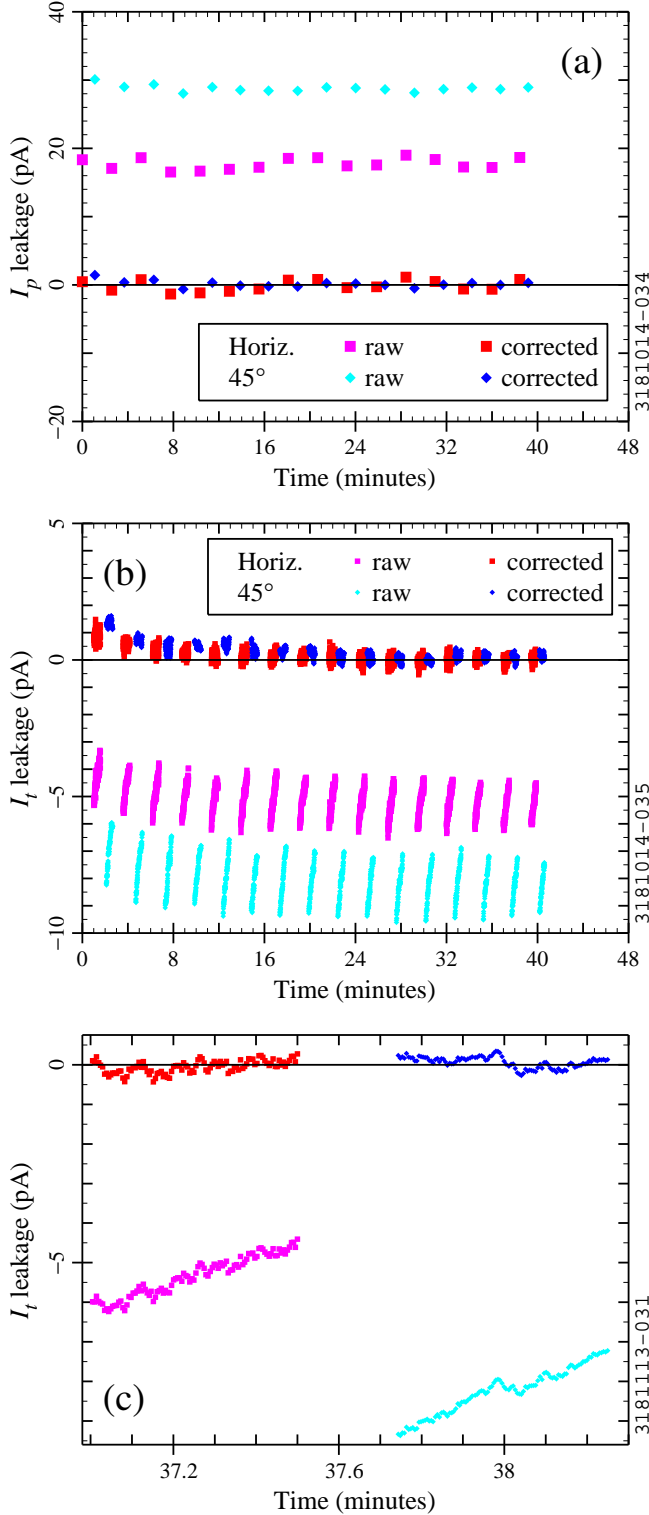


**Figure 15.** Example of measurements of leakage current as a function of time while switching the bias voltage. (a) Leakage measurements with  $V_b = +150$  V for  $I_p$  correction (1 point per iteration); (b) leakage measurements with  $V_b = -20$  V for  $I_t$  correction (120 points per iteration); (c) same as (b), but zoomed in for a better view of the penultimate iteration. Light colors (magenta and cyan) indicate uncorrected values and dark colors (red and blue) indicate corrected values. The measurements were done in August 2012 with stainless steel samples.

for the SEY scans. The current changes by 2 to 3 pA during the measurement, which is about 2% of  $I_p$  for Phase II parameters.

The darkly-colored markers (red and blue) in Figure 15 show the result of applying the time-dependent leakage correction described in Section D.3. Over most of the scan, the corrected current is  $\pm 1$  pA or less, which is about 1% of  $I_p$ , comparable to the leakage current drift (Section 5.5). There are larger discrepancies during the first few minutes of the scan, which are likely due to the need for iterations to reach a stable current (Section 5.5).

As can be seen in Figure 15b, the time-dependent correction compensates for the transient behaviour reasonably well. Zooming in on one iteration (Figure 15c), we see that the corrected current differs from zero, but the systematic differences are comparable to the noise in the measurement.

The time-dependent correction is based on the recorded time stamp for each current measurement, so that variations in the time per grid point and the adjustments in the waiting time to avoid cross-talk (Section 5.10) are taken into account. This has the added advantage that we can still apply the leakage correction procedure even if the timing and scanning parameters are not exactly the same for the leakage scan and the SEY scan.

The measurements shown in Figure 15 were taken over the same time interval, with measurements at positive and negative bias interleaved, and with a time offset between the horizontal and 45° stations. The time is measured relative to the first current measurement for the horizontal station.

The SEY is calculated from  $I_p$  and  $I_t$  using Equation (2). Because the numerator and denominator are both corrected, the effect on the SEY can be partially cancelled. For example, if the uncorrected and corrected  $I_t$  values are small relative to  $I_p$ , SEY is approximately 1 and the corrections to  $I_p$  do not produce much change in the SEY. Figure 16 shows examples of the current correction's impact on the SEY values. For unconditioned Al with a peak SEY of approximately 2.5 (Figure 16a), the correction increases the peak by about 10%. For reconditioned TiN with a peak SEY close to 1 (Figure 16b), the correction decreases the peak by about 5%.

In Figure 16, both the first (solid curves) and the repeated (dashed curves) measurements are shown, since this grid point is measured twice in the double scan; the first and second  $I_t$  measurements are separated in time by  $\sim 17$  s. The  $I_t$  values are corrected by different amounts to account for the current transient. However, there is little difference in SEY, which indicates that the variation in  $I_t$  over the time required to scan the grid points has little impact on SEY.

Thus, in the examples above, the magnitude of the leakage current is approximately 15% of  $I_p$  or less, which is typical for the Phase II measurements with leakage mitigation; the unmitigated leakage current could be 100% of  $I_p$  or more under adverse conditions. The correction to the measured SEY due to the leakage current is approximately 10% or less, which is also typical for Phase II measurements. With 120 grid points, there is a clear time dependence in the leakage current due to the bias switch transient. The time-dependent leakage correction accounts for this effectively, but the impact on the measured SEY is small for the Phase II SEY scans, in which we

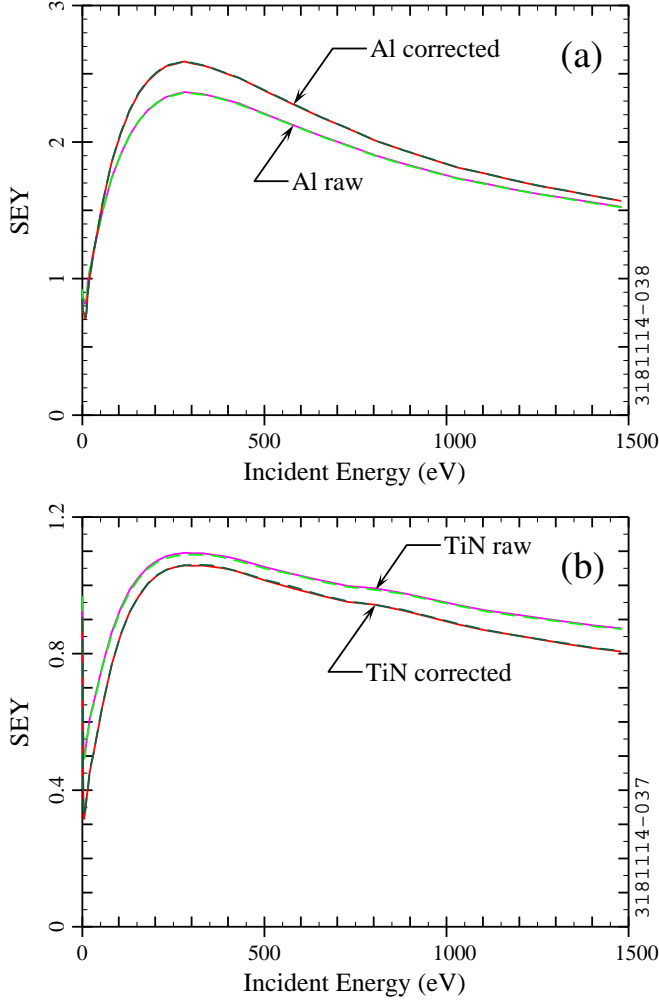


**Figure 16.** Example of measurements of SEY as a function of energy without correction (light colors) and with correction for leakage current and transient response (dark colors): (a) unconditioned Al measured in January 2013; (b) reconditioned TiN measured in November 2012. Both the first measurement (solid curves) and second measurement (dashed curves) are shown. All values are for the middle grid point of the 45° sample ( $\theta = 25^\circ$ ).

used a wait time after a bias switch of  $t_{bw} = 60$  s. Hence it may be possible to shorten the wait time in future measurements. (However, as discussed in Section 5.10, with the Phase IIb parameters, there is little timing margin to avoid cross-talk; hence a different cross-talk avoidance method would be needed if we were to decrease  $t_{bw}$  significantly.)

#### 6.4. Uncertainties

As discussed above, a number of modifications for Phase II were oriented toward reducing the systematic errors in the measurements. Table 3 summarises the estimated contributions to the systematic error from various sources for various measurement scenarios. The values apply to both  $I_p$  and  $I_t$  measurements, but they are expressed as a percentage of  $I_p$  (it is not straightforward to estimate the error as a fraction of  $I_t$ ).

Using Equation (2), one can infer the impact of errors in the measurement of  $I_p$  and  $I_t$  on the calculated SEY. For Phase IIb,

**Table 3.** Summary of estimated current measurement errors as a percentage of  $I_p$ . For errors due to leakage and transient currents, the Phase II value of  $I_p \sim 200$  pA is assumed; the estimated errors would be smaller for Phase I, since  $I_p$  was  $\sim 2$  nA. The scenarios used for the final Phase II procedure are in bold type. HH = high humidity, LH = low humidity (as quantified in Section E.1), SC = static correction, TDC = time-dependent correction.

Source	Mitigate?	Correct for?	Error
Gun current drift (§5.2)	no (Ph. I)	no	$\lesssim 16\%$
	<b>yes (Ph. II)</b>	<b>no</b>	<b><math>\lesssim 2\%</math></b>
Leakage current (§5.4–5.5)	no (HH)	no	$\gtrsim 100\%$
	no (LH)	no	$\lesssim 14\%$
	no (HH)	yes	$\gtrsim 100\%$
	no (LH)	yes	$\lesssim 1\%$
	<b>yes</b>	<b>no</b>	$\lesssim 14\%$
Transient current (§5.6, §6.3)	<b>yes</b>	<b>yes</b>	<b><math>\lesssim 1\%</math></b>
	no ( $t_{bw} = 0$ )	no	$\gtrsim 100\%$
	yes ( $t_{bw} = 60$ s)	no	$\lesssim 4\%$
	yes ( $t_{bw} = 60$ s)	yes (SC)	$\lesssim 2\%$
Cross-talk (§5.10)	yes ( $t_{bw} = 60$ s)	<b>yes (TDC)</b>	<b><math>\lesssim 1\%</math></b>
	no (Ph. IIa)	no	$\lesssim 50\%$
	<b>yes (Ph. IIb)</b>	<b>no</b>	<b>none</b>

we expect the items listed in Table 3 to produce a systematic error in SEY of at most a few percent for  $0 \leq \text{SEY} \leq 2$ .

Estimates of errors due to charging and conditioning are not included in Table 3. From Figure 10, we infer that the error in the calculated SEY due to charging was  $\sim 45\%$  for DLC with the Phase I method. With the Phase IIb method, as discussed in Section 5.3, our observations indicate that there is some charging or conditioning of unconditioned and susceptible materials at the parking point (decreasing the measured SEY by  $\lesssim 7\%$  with mitigation). We will return to the discussion of errors due to conditioning in Section 7.4.

Overall, we expect the items considered in Section 5 to contribute a few percent to the systematic error in the SEY for most grid points (and  $\lesssim 10\%$  for the parking point) with the Phase IIb method. We estimate that the statistical errors are of the same order. A future paper will include more detailed results with a more complete error analysis.

## 7. Examples of SEY Results

Some examples of SEY measurements with the in-situ stations are presented in this section. The beam dose to the samples is calculated in terms of the integrated current of stored electron bunches; for a beam energy of 5.3 GeV, 1 ampere-hour corresponds to about  $3 \cdot 10^{21}$  photons/m of direct synchrotron radiation at the location of the SEY samples. As discussed above, the horizontal sample is oriented to receive direct SR photons, but the 45° sample receives only scattered photons (though both samples may be conditioned by electrons from the cloud).

### 7.1. SEY as a Function of Energy

Figure 17 shows the measured SEY of the 45° diamond-like-carbon-coated sample as a function of energy for different

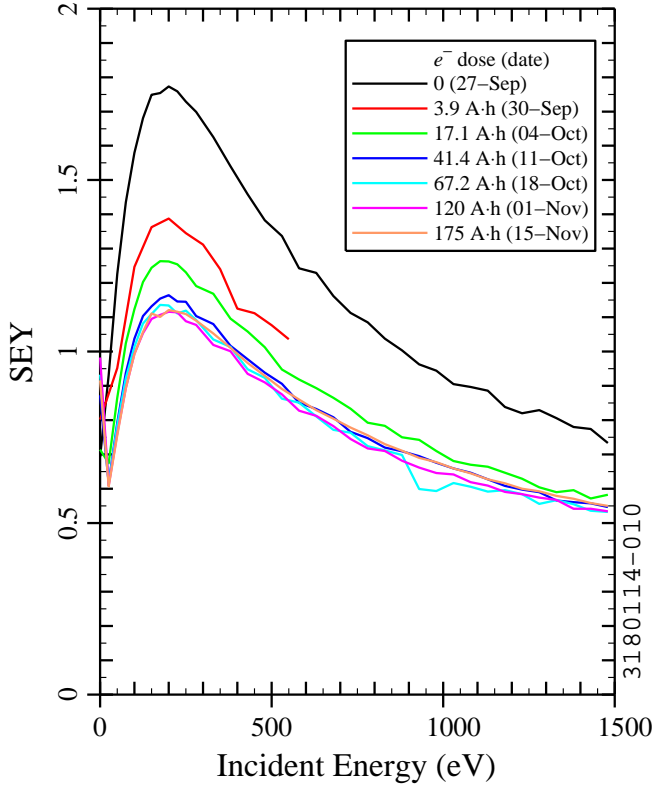


**Figure 17.** SEY as a function of incident energy for the 45° diamond-like carbon sample. The values shown are for the grid point in the middle of the sample, which has  $\theta = 25^\circ$ . The sample was exposed to the beam pipe environment during Phase IIa from September 2011 to November 2011. The second measurement (red curve) was stopped early due to time constraints.

beam doses. The measurements indicate a peak in the SEY at about 200 eV. There is a clear decrease in the SEY as a function of beam dose. Before conditioning, the peak SEY is about 1.8; for beam doses greater than 20 ampere-hours, the peak SEY is significantly lower, in the range of 1.1 to 1.2. The observed changes due to conditioning are large compared to the estimated errors in the measurement.

### 7.2. Peak SEY as a Function of Vertical Position

Figure 18 shows measurements of the peak SEY as a function of vertical position for stainless steel. The gun deflection angle is converted to azimuthal angle along the inside of the beam pipe. The coordinate system is such that the middle of the horizontal sample is at zero and the middle of the 45° sample is at  $-45^\circ$ .

Figure 18a compares different beam doses. Before beam exposure (black), the peak SEY is about 1.8 and is approximately constant. After a small beam dose (red), a dip in the SEY appears near the middle of the horizontal sample, presumably due to photon bombardment from direct SR. For high doses, the SEY decreases and returns to being approximately independent of position. The measurements thus suggest that direct SR produces rapid conditioning, while conditioning by scattered photons and/or electrons happens more slowly. In the stainless steel

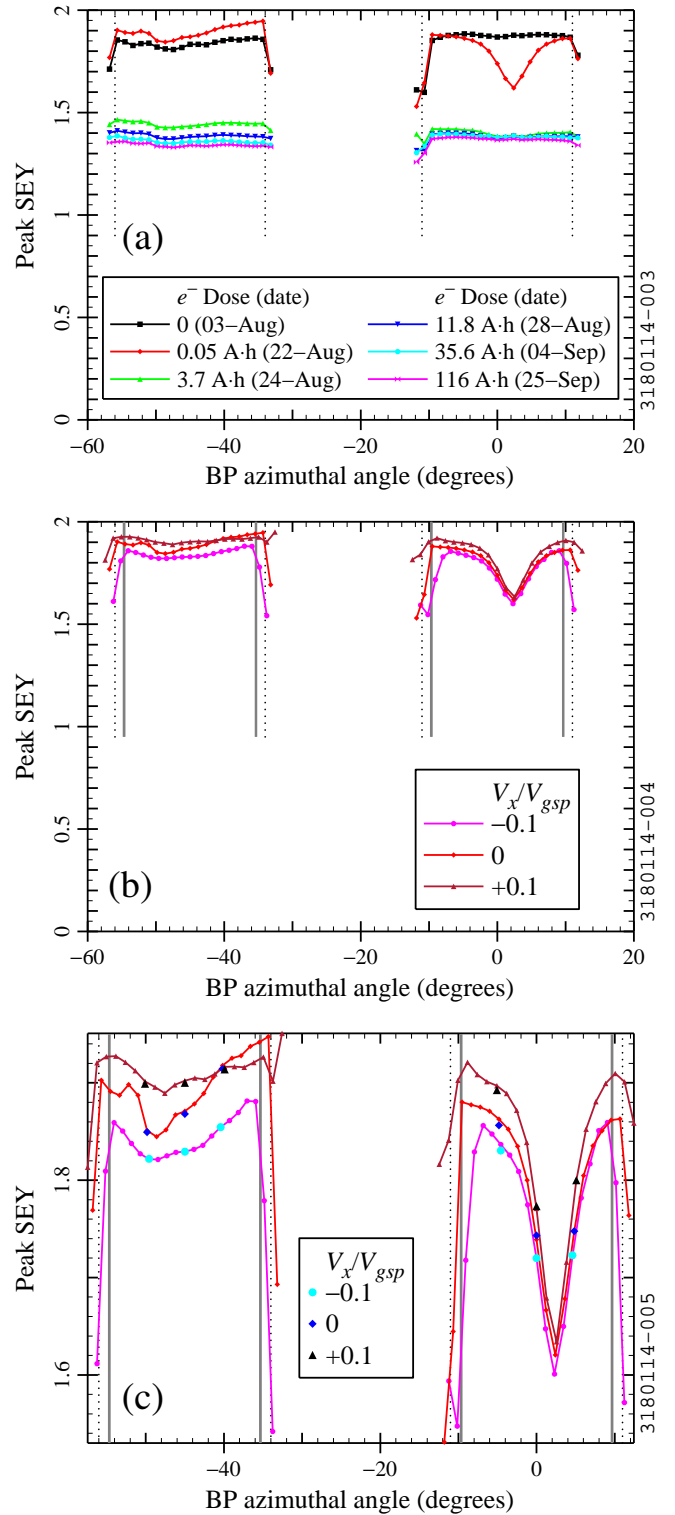


**Figure 18.** Peak SEY of stainless steel samples as a function of position expressed in terms of the azimuthal angle along the beam pipe (BP). (a) Scans along the middle of the sample ( $\theta \approx 25^\circ$ ) for different beam doses; (b) scans along the left, middle, and right of the sample for the 0.05 A·h case; (c) zoomed-in version of (b) with repeated points from the double scan included. The black dotted lines indicate the edges of the sample for the middle deflection scan; the solid gray lines correspond to the sample edges for the left and right deflection scans. The measurements were done in Phase IIb from August 2012 to September 2012.



case, little difference is seen except for the lowest dose (which is a small fraction of the typical weekly beam dose with CHES current). The observed differences due to beam scrubbing are again large compared to the estimated errors in the measurement.

As described in Section 5.8, double scans are done for 3 different values of the horizontal and vertical deflection. Figure 18b compares the peak SEY as a function of position for 3 different horizontal deflections (grid points with square markers in Figure 12) for the 0.05 A-h case (the red case in Figure 18a). The dip near the middle of the horizontal sample is seen in all 3 scans. Figure 18c shows a zoomed-in version of Figure 18b with additional values for repeated grid points included, as will be discussed in Section 7.4. The values in Figure 18b and Figure 18c are labelled according to the relative horizontal deflection,  $V_x/V_{gsp}$ , which is defined in Section B.3.

### 7.3. Peak SEY as a Function of Incident Angle

Figure 19 shows the peak SEY as a function of incident angle for the measurements on stainless steel described in the previous section. The results are based on scanning the horizontal deflection and converting to the angle of incidence  $\theta$  relative to the sample's surface normal. (Hence, the position and the angle are both varying.) The incident angle is  $25^\circ$  in the middle of the sample. Only the  $45^\circ$  sample is shown.

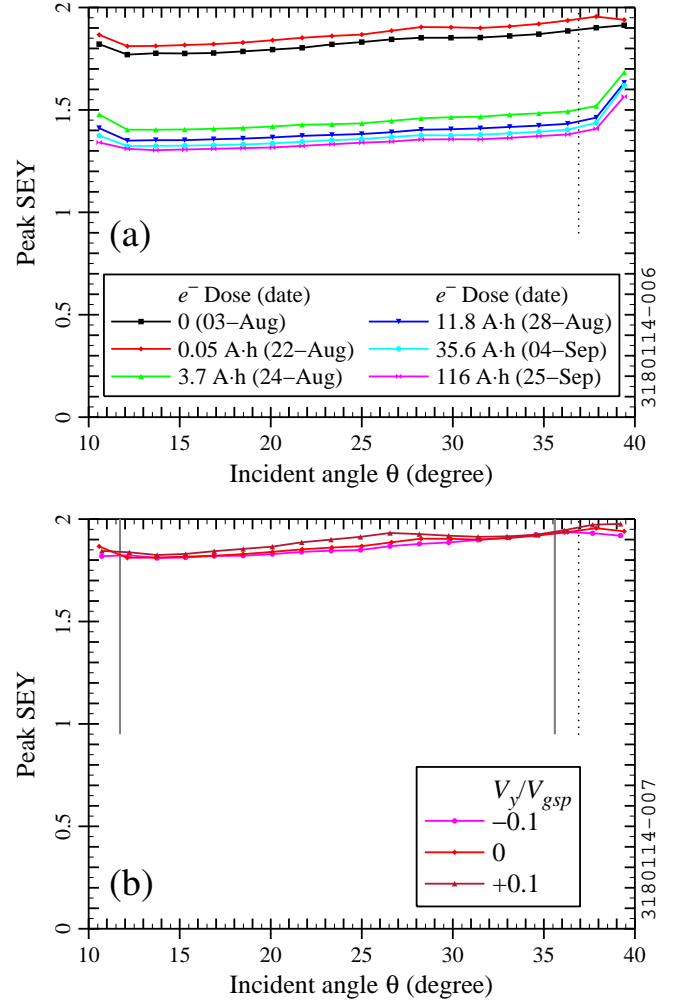
Figure 19a compares different beam doses. Consistent with the left side of Figure 18a, the peak SEY decreases with increasing beam dose. There is a slight increase in SEY with increasing angle, which is qualitatively consistent with what one would expect—generally, the SEY has been observed to increase as the primary beam's angle changes from normal incidence to grazing incidence.

Figure 19b compares the peak SEY as a function of angle for 3 different vertical deflections (grid points with diamond markers in Figure 12) for the 0.05 A-h case. There is some variation from one vertical deflection to another, but all cases show a similar increase in SEY with increasing  $\theta$ . The consistency between different vertical positions and different beam doses suggests that our measurements are able to resolve the angular dependence of the SEY, though the differences are not very large compared to the estimated errors in the measurement.

The curves in Figure 19b are labelled according to the relative vertical deflection,  $V_y/V_{gsp}$  (defined in Section B.3). As discussed in Section 5.3, the integrated flux from the electron gun is highest for the parking point. The parking point has  $V_x/V_{gsp} = +0.1$  (corresponding to  $\theta \approx 31.5^\circ$ ) and  $V_y/V_{gsp} = +0.1$ . As can be seen in Figure 19b, there is no evidence of additional conditioning at the parking point for stainless steel.

### 7.4. Reproducibility

As discussed in Section 5.8, nine grid points are measured twice in the double scan (shown by overlapping squares and diamonds in Figure 12). This provides a way to check the reproducibility of the SEY measurement over short time intervals. In Figure 18c, the scans along the 3 different horizontal lines from Figure 18b are shown in a zoomed-in view (in shades of red),



**Figure 19.** Peak SEY of the  $45^\circ$  stainless steel sample as a function of incident angle relative to the surface normal. (a) Scans along the middle of the sample for different beam doses; (b) scans along high, middle, and low lines along the sample for the 0.05 A-h case. The black dotted lines indicate the edges of the sample for the middle deflection scan; the solid gray lines correspond to the sample edges for the high and low deflection scans. The measurements were simultaneous with the measurements of SEY as a function of position shown in the previous figure.

with additional values for the repeated grid points included (in black and shades of blue). In both cases, the colors range from light to dark as the horizontal deflection ranges from negative to positive. The values from the repeated measurement are reasonably consistent. This suggests that the features in the vertical position scans are reproducible and that the system is able to properly resolve the dependence of SEY on position.

We are not able to repeat the in-situ SEY measurements routinely, but we can occasionally during extended access periods. Repeated measurements on Al samples (1 or 2 days apart, without intervening exposure to beam) in Phase II indicate that the measured SEY can vary by up to 5% or more for a few grid points. For most of the 120 grid points, the SEY varies by a few percent or less. Thus the measured changes with beam exposure are large compared to the day-to-day reproducibility of the measurements. The reproducibility is consistent with what

we expect based on the systematic uncertainties discussed in [Section 6.4](#).

## 8. Conclusion

We have developed an in-situ secondary electron yield measurement system to observe conditioning of metal and coated samples by CESR beams. Our system allows for the measurement of SEY as a function of incident electron energy, position on the sample, and incident electron angle. Our experience with the initial measurements led us to implement improvements in the method to reduce charging and conditioning by the electron gun; mitigate and correct for the leakage current and transient current; eliminate cross-talk between the adjacent SEY stations; and mitigate the slow drift in the electron gun current. We have reduced the contributions to the systematic error from these effects to a few percent, allowing us to measure the dependence of the SEY on beam dose, incident angle, and position with better resolution. In-situ measurements have been carried out on a number of materials. Preliminary results have been reported previously, and will be presented in more detail in a future paper.

SEY models generally divide the secondaries into elastic, rediffused, and true secondaries. Our measurement technique is well-suited to the low-energy true secondaries, but not as well-suited to the higher-energy rediffused and elastic secondaries. Hence, we expect to be able to extract reasonable model parameters for the true secondary contribution (as will be presented in a future paper), but we expect more uncertainty in the model parameters of the rediffused and elastic contributions.

There is room for additional improvements in the SEY measurement techniques. Sources of systematic error that we have not yet accounted for include (i) the escape of elastic and rediffused secondaries when the sample is positively biased to measure the primary current, and (ii) the deflection of electrons by the sample bias in the case of primary electrons with a small incident energy. Our progress with (ii) is important to our goal of finding SEY model parameters that are reliable for incident electrons of low energies. A more direct measurement of the primary and/or secondary current may help reduce some of the systematic error. We would like to gather additional information about the energy distribution of the secondary electrons, in order to distinguish true secondaries, rediffused secondaries, and elastic secondaries. Additional improvements to the measurement apparatus and techniques might allow us to reduce the measurement time and decrease the incidence of noise spikes in the current due to nearby activity. Some of the improvements described above may not be practical for our in-situ apparatus, and may have to be implemented with a more advanced out-of-tunnel SEY measurement system.

Our ultimate goal is to use the SEY measurements under realistic conditions to constrain the SEY model parameters as much as possible; this will help improve the predictive ability of models for electron cloud build-up, allowing for more successful electron cloud mitigation in future accelerators to help them achieve better performance and higher reliability.

## Acknowledgments

We are grateful for the support of collaborators at SLAC, who provided hardware, samples, and guidance for the SEY studies at CESR-TA. Amorphous carbon coating and diamond-like carbon coating of samples was done by CERN and KEK, respectively. We thank our collaborators at Fermilab for useful discussions.

Our work would not have been possible without the support of personnel in the design, electronics, fabrication, information technology, operations, survey, technical services, and vacuum groups. We are particularly thankful for the work by V. Medjidzade and the support from W. J. Edwards, B. M. Johnson, J. A. Lanzoni, R. Morey, and R. J. Sholtys. We thank our CESR-TA collaborators for their support, ideas, and encouragement, particularly J. R. Calvey, J. A. Crittenden, G. F. Dugan, J. P. Sikora, and K. G. Sonnad. S. T. Wang provided valuable help and guidance with our data acquisition program development work. We thank S. B. Foster for doing off-line SEY measurements and helping with in-situ measurements. We appreciate the support from the CESR and laboratory management for our studies, particularly from M. G. Billing, D. H. Rice, D. L. Rubin, J. W. Sexton, and K. W. Smolenski.

This work was supported by the National Science Foundation through Grants PHY-0734867 and PHY-1002467 and by the Department of Energy through Grants DE-FC02-08ER-41538 and DE-SC0006505.

## Appendix A. Current Control and Measurement

### A.1. Electron Gun Current Control

The cathode power (adjusted via the cathode voltage,  $V_{source}$ ) provides the primary method of controlling the electron gun current. The Wehnelt potential (grid bias, referred to as  $G_1$  by the gun manufacturer) and first anode potential (referred to as  $G_2$  by the manufacturer) provide additional control over the gun parameters, including the current; the current decreases with  $G_1$  and increases with  $G_2$ . For our SEY measurements, we establish the desired electron gun current by applying a constant voltage across the cathode filament ( $V_{source} = 1.2$  V) and setting  $G_1$  and  $G_2$  values of order 16 V and 100 V, respectively; the values of  $G_1$  and  $G_2$  vary by a few percent from one measurement to another in order to get the desired gun current.

The electron gun power supply has a beam current read-back and an “emission control” feature in which a feedback loop adjusts the source voltage to make the gun current read-back equal to a set point value. However, for our parameters, we found that the feedback loop went unstable after an energy step. As a result, all of the SEY measurements have been done with the feedback loop turned off.

For low-current SEY measurements (see [Section 5.3](#)), the gun current is too low for an accurate read-back value. Even at higher currents, we sometimes observe that the gun current read-back is inaccurate. As a result, we generally rely on the sample current as measured by the picoammeter for the SEY measurements rather than the gun current read-back.

### A.2. Electron Gun Current Modulation

As discussed in Section 5.3, in Phase IIb, we decreased the electron gun current while waiting for the sample current to stabilize after a change in the bias. This is done by raising  $G_1$ , rather than by decreasing  $V_{source}$  (had we adjusted  $V_{source}$ , we would have had to account for the thermal time constant of the cathode and would have likely worsened the long-term stability of the cathode emission characteristics). During each 60-second waiting period after a change in bias, we increase  $G_1$  by 1 volt. The increase in  $G_1$  produces a decrease in the gun emission current by about a factor of 4. The choice of  $\Delta G_1 = 1$  V is a compromise between our desire for a large change in  $G_1$  to minimise the dose and our desire to keep  $\Delta G_1$  small for stable gun current. With  $\Delta G_1 = 1$  V, we found that the gun current stabilises within about 7 seconds after the step in  $G_1$ . This was the basis for returning to the nominal value of  $G_1$  for a time  $t_{cw} = 10$  s before starting the measurement (Figure 8).

### A.3. Current Measurement Parameters

As described in Section 5.9, the picoammeter parameters were adjusted in Phase II to avoid unintentional averaging over grid points. The picoammeters average the current internally and provide the averaged value to the data acquisition program. The picoammeters can be set for either a “moving average” without hand-shaking or a “repeated average” with hand-shaking. The time required per measurement is the product of the integration time of the analog to digital converter and the number of points to be averaged. The parameters for the Phase I and Phase IIb measurements are shown in Table 4.

**Table 4.** Picoammeter parameters for Phase I and Phase IIb.

Phase	I	IIb
Integration time	$\frac{1}{10}$ s (slow)	$\frac{1}{60}$ s (med.)
Average type	moving	repeated
Hand-shaking	no	yes
Measurements	10	10
Time needed per grid point	1 s	$\frac{1}{6}$ s

## Appendix B. Parameters for Scanning the Energy, Focus, and Deflection

### B.1. Energy Segments

A variable energy step was used in Phase II for better energy resolution at low energies (Section 5.7). The energy segments for variable-step SEY scans are listed in Table 5.

### B.2. Focus as a Function of Energy

The electron gun focussing voltage is adjusted as a function of electron gun energy to produce a minimum electron beam spot size on the sample (Section 3.5). The set point values are shown in Figure 20.

**Table 5.** Electron gun energy segments for SEY scans with a variable energy step. A total of 44 energies are measured.

Interval	Start	End	Step	Points
1st	20 eV	25 eV	1 eV	6
2nd	25 eV	35 eV	2 eV	5
3rd	35 eV	50 eV	5 eV	3
4th	50 eV	450 eV	25 eV	16
5th	450 eV	1500 eV	75 eV	14

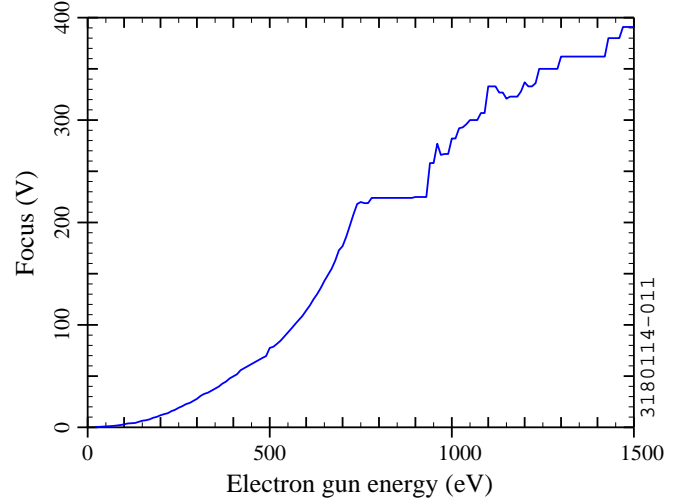


**Figure 20.** Set point focussing voltage as a function of electron gun energy.

### B.3. Deflection Parameters

Paired electrostatic plates deflect the electrons to the desired horizontal angle ( $\alpha_x$ ) and vertical angle ( $\alpha_y$ ) relative to the gun axis. The deflection set point is specified by the voltages  $V_x$  and  $V_y$  to be applied to the deflecting electrodes. The  $x$  deflection angle,  $x$  deflection voltage, and gun energy set point  $K_{gsp} = q_e V_{gsp}$  are related by

$$\tan(\alpha_x) = g \frac{V_x}{V_{gsp}}, \quad (5)$$

where  $g$  is a constant that depends on the spacing and length of the deflecting electrodes ( $q_e$  = the electron charge magnitude). The relationship between  $\alpha_y$  and  $V_y$  is analogous. For our electron gun model,  $g = \frac{40}{3} \tan(4.9^\circ)$ . We checked the above relationship using a phosphor screen to view the electron beam spot.

Two arrays of grid points were used for better spatial range and resolution (Section 5.8). The deflection parameters for the double scans are given in Table 6. Per Equation (5), the deflecting voltages must be scaled with the set point energy  $K_{gsp} = q_e V_{gsp}$ . The relative horizontal deflection  $V_x/V_{gsp}$  is incremented from  $-(V_x/V_{gsp})_{max}$  to  $+(V_x/V_{gsp})_{max}$  with a given step size; the relative vertical deflection  $V_y/V_{gsp}$  is incremented similarly. The relative deflection step is 0.025 at high resolution and 0.1 at low resolution. The desired step size and range determines the dimensions of the array ( $n_x$  by  $n_y$ ). As shown in Figure 12,

**Table 6.** Grid parameters for double scans.

Standard Double Scan				
Array	$n_x$	$n_y$	$(V_x/V_{gsp})_{max}$	$(V_y/V_{gsp})_{max}$
1	3	21	0.1	0.25
2	19	3	0.225	0.1
High Definition Double Scan				
Array	$n_x$	$n_y$	$(V_x/V_{gsp})_{max}$	$(V_y/V_{gsp})_{max}$
1	3	3	0.1	0.1
2	19	21	0.225	0.25

the arrays overlap, resulting in some grid points being measured twice.

Some additional measurements are done with a “high definition” array (along with a low definition array which provides the same duplication of points as for the standard double scan). The deflection parameters for high definition scans are also included in Table 6.

## Appendix C. Collimation Slit Measurements

As discussed in Section 3.5, collimation measurements were done to determine the focus setting as a function of beam energy to produce an approximate minimum in the beam spot size and estimate the minimum spot size as a function of energy. Furthermore, as described in Section 2.5, the collimation measurements provided a way to check the magnetic shielding of the system.

In the collimation measurements, the sample was biased with +20 V and was used as a Faraday cup. A collimator with a 1 mm slit was electrically isolated from the sample and centered in front of the sample, with the slit oriented in the vertical ( $y$ ) direction. With the electron gun at the nominal distance from the sample (32.9 mm), two picoammeters were used to measure the electron currents reaching the collimator and the sample.

### C.1. Focus and Beam Spot Size

At each electron beam energy, the gun’s focusing voltage was varied to find the focus to produce the maximum current to the sample and the minimum current to the collimator. These measurements provided the basis for the set point focus values used in the SEY measurements and shown in Figure 20.

Figure 21 shows the current passing through the slit and reaching the sample divided by the total current (current to sample plus current to collimator) as a function of energy with the focus set as described above and without  $x$  deflection. For beam energies between 200 eV and about 800 eV, nearly all of the current reaches the sample, indicating that the beam spot size is smaller than 1 mm. Outside this energy range, some of the current is intercepted by the collimator. These results are the basis for the beam size estimates given in Section 3.5; we assumed a Gaussian beam distribution based on the specifications provided by the electron gun manufacturer.

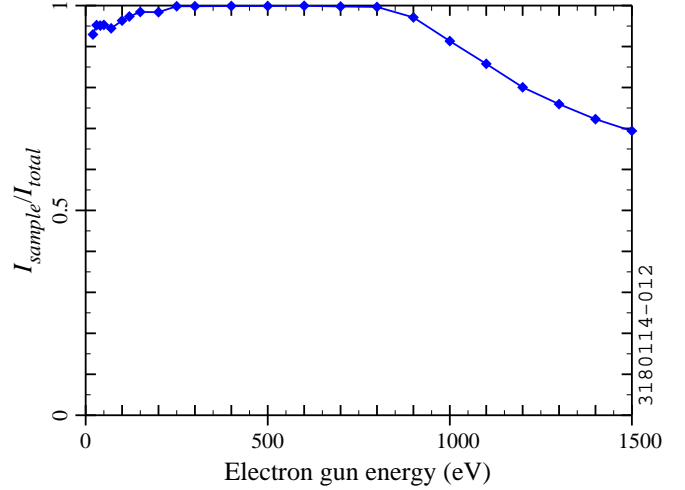


**Figure 21.** Slit collimation measurements for the SEY system. For the vertical axis,  $I_{sample}$  is the current reaching the sample and  $I_{total}$  is the current reaching the sample plus the current reaching the collimation electrode.

We attempted to do a more direct measurement of the beam spot size using a phosphor screen. However, we found that the beam spot was not visible except at high electron beam energies with high electron beam current. As a result, we relied on the method described above instead.

### C.2. Deflection Check

At each energy, the beam was scanned across the slit using the gun’s horizontal ( $x$ ) deflection electrode to find the deflection value for maximum current to the sample and minimum current to the collimation electrode (corresponding to the beam passing through the middle of the slit). Over the full range of electron beam energy (0 to 1500 eV), the value of the  $x$  deflection voltage to center the beam spot on the slit was zero, which confirms that the stray magnetic field is well shielded.

## Appendix D. Model for Time-Dependent Correction of Leakage Current and Current Transients

As indicated in Section 6.3, with a large number of grid points, we observed that the leakage current was changing slowly in the time required to measure  $I_t$  for all of the points. This provided the motivation to develop a model for the leakage current that accounted for the transient current.

### D.1. Simple Measurements; Semi-Empirical Model

Our first approach was to develop a relatively simple circuit model with a voltage source representing the picoammeter’s biasing power supply; a series resistance  $R_s$  between the power supply and the sample; a resistance  $R_{||}$  between the sample and ground to produce a leakage current; and a capacitance  $C_{||}$  from the sample to ground to produce a transient current. Unsurprisingly, this circuit’s response to a step in the power supply voltage is a transient current which decays exponentially in time to a steady-state current.



To evaluate the usefulness of the circuit model, we measured the sample current  $I$  as a function of time  $t$  after stepping the bias voltage. Figure 22a shows the current as a function of time for the 45° SEY system for simple cases, stepping the bias voltage between  $V_b = 0$  and  $V_b = \pm 150$  V. The approximate time at which the bias is stepped ( $t_1$ ) is subtracted from  $t$ . The measured transient current is as high as about  $\pm 500$  pA, which is much larger than the steady-state current of  $\pm 15$  pA or less.

In Figure 22b, we subtract the approximate steady-state current ( $I_\infty$ ) from  $I(t)$  and we zoom in for a more clear view of the current for  $t - t_1 > 20$  seconds. Additionally,  $I - I_\infty$  is multiplied by a sign correction coefficient  $s = \pm 1$  to compare the transients associated with upward and downward steps in  $V_b$  on the same footing. For our present method, the time interval of interest for SEY measurements starts 60 seconds after the bias step and, in the case of the double scan, lasts for 35 seconds. The dotted vertical lines in Figure 22b delimit this time interval. (For high definition double scans, the measurement takes 118 seconds.)

The values of  $I_\infty$  are given in the caption of Figure 22. Ideally, we should have  $I_\infty = 0$  when  $V_2 = 0$  and the same value of  $|I_\infty|$  when  $V_2 = \pm 150$  V, but the best-match results vary by 1 pA, which presumably is indicative of small offsets in the system.

Since the circuit model predicts that the current  $I$  should decay exponentially towards its steady state value  $I_\infty$ , a linear-log plot of  $I(t) - I_\infty$  versus  $t - t_1$  should produce a straight line. However, as shown in Figure 22c, the measured current has a distinctive curvature on linear-log scales. This indicates that the current does not decay exponentially to its steady-state value as predicted by the circuit model. Our inference is that the picoammeter is an active element of the circuit, not a passive element as assumed for the circuit model.<sup>16</sup>

Figure 22d shows a log-log plot of  $I(t) - I_\infty$  versus  $t - t_1$ . For  $t - t_1 > 30$  seconds, the relationship is approximately linear. The solid cyan line of Figure 22d follows the simple form

$$I(t) - I_\infty = \frac{A}{t - t_1}, \quad (6)$$

where  $A$  is a constant. The cyan curves in Figure 22b and Figure 22c represent the same function as the cyan line of Figure 22d. Based on considerations from the circuit model, we expect  $A$  and  $I_\infty$  to be constants for given values of the initial and final bias, with  $I_\infty$  being approximately proportional to the final bias voltage and  $A$  being approximately proportional to the voltage step.

Figure 22d shows that the measured current differs significantly from the cyan line of Equation (6) for  $t - t_1 < 30$  seconds; the model in fact predicts an infinite current for  $t - t_1 \rightarrow 0$ ; however, we are searching for a model which can be applied for  $t - t_1 \geq 60$  seconds, so the discrepancies for  $t - t_1 < 30$  seconds are not a problem for us in practice.

Denoting the initial bias as  $V_0$  and the final bias as  $V_2$ , and taking into account the above comments about  $A$  and  $I_\infty$ , we

can formulate Equation (6) as

$$I(t) = \Gamma_{\parallel} \left( \frac{V_2 - V_0}{t - t_1} \right) + \frac{V_2}{R_{\parallel}}, \quad (7)$$

where  $\Gamma_{\parallel}$  and  $R_{\parallel}$  are constants. For  $t \rightarrow \infty$ ,  $I(t) \rightarrow I_\infty = V_2/R_{\parallel}$ , consistent with the simple circuit model with resistance  $R_{\parallel}$  between the sample and ground (for  $R_s \ll R_{\parallel}$ ). The constant  $\Gamma_{\parallel}$  has dimensions of capacitance, and can be thought of as being a “capacitance-like” quantity, even though Equation (7) does not represent the transient behaviour of an RC circuit.

The values of the model parameters corresponding to the cyan curves in Figure 22 are given in Table 7. Measurements of the current as a function of time after a voltage step were done on the horizontal station and the off-line station, in addition to those on the 45° station reported above. The measured currents for the other stations were found to be consistent with the semi-empirical relation of Equation (7), although the horizontal system’s current was a bit more noisy. The model parameters for the other systems are also included in Table 7.

**Table 7.** Values of the semi-empirical model parameters for the SEY stations inferred from the measured current as a function of time after a voltage step.

Station	$\Gamma_{\parallel}$	$R_{\parallel}$
Horizontal	2.0 pF	15.8 TΩ
45°	2.5 pF	10.4 TΩ
Off-line	2.5 pF	14.6 TΩ

## D.2. Realistic Measurements; Additional Considerations

To test the applicability of the semi-empirical model to a more realistic case, we did additional measurements in which we switched the bias between  $-20$  V and  $+150$  V, as is done for SEY scans. Figure 23 shows results for the 45° system. The behaviour is similar to that of the simpler cases discussed above. The cyan curves represent the semi-empirical model, which, as above, fits the measurements reasonably well when  $t - t_1 > 30$  seconds. The best match corresponds to model parameters of  $\Gamma_{\parallel} = 2.3$  pF and  $R_{\parallel} = 10$  TΩ, values that are slightly different from those given in Table 7.

The results for the horizontal system and the off-line system are not shown, but the behaviour was similar. The best-match parameters were similar to the values of Table 7. In the case of the off-line system, we observed that a non-integer power relation of the form  $I(t) - I_\infty \sim (t - t_1)^{0.85}$  produced a better fit than Equation (7), but we chose to keep the semi-empirical model simple rather than introduce additional parameters.

Although the model parameters obtained by switching between more realistic bias values are slightly different from the values in Table 7 based on more simple measurements, they are all consistent with the model parameters inferred from leakage scans, which show some long-term variation in time (see Section E.2 and Figure 26 below).

For the simple circuit model, the sample bias is not equal to the power supply bias in general, but, if the series resistor

<sup>16</sup>The picoammeter has settings for “damping on” and “damping off” which affect its time response. We found that neither setting gives an exponential decay in the transient current. All of the SEY scans were done with the default setting of damping on.

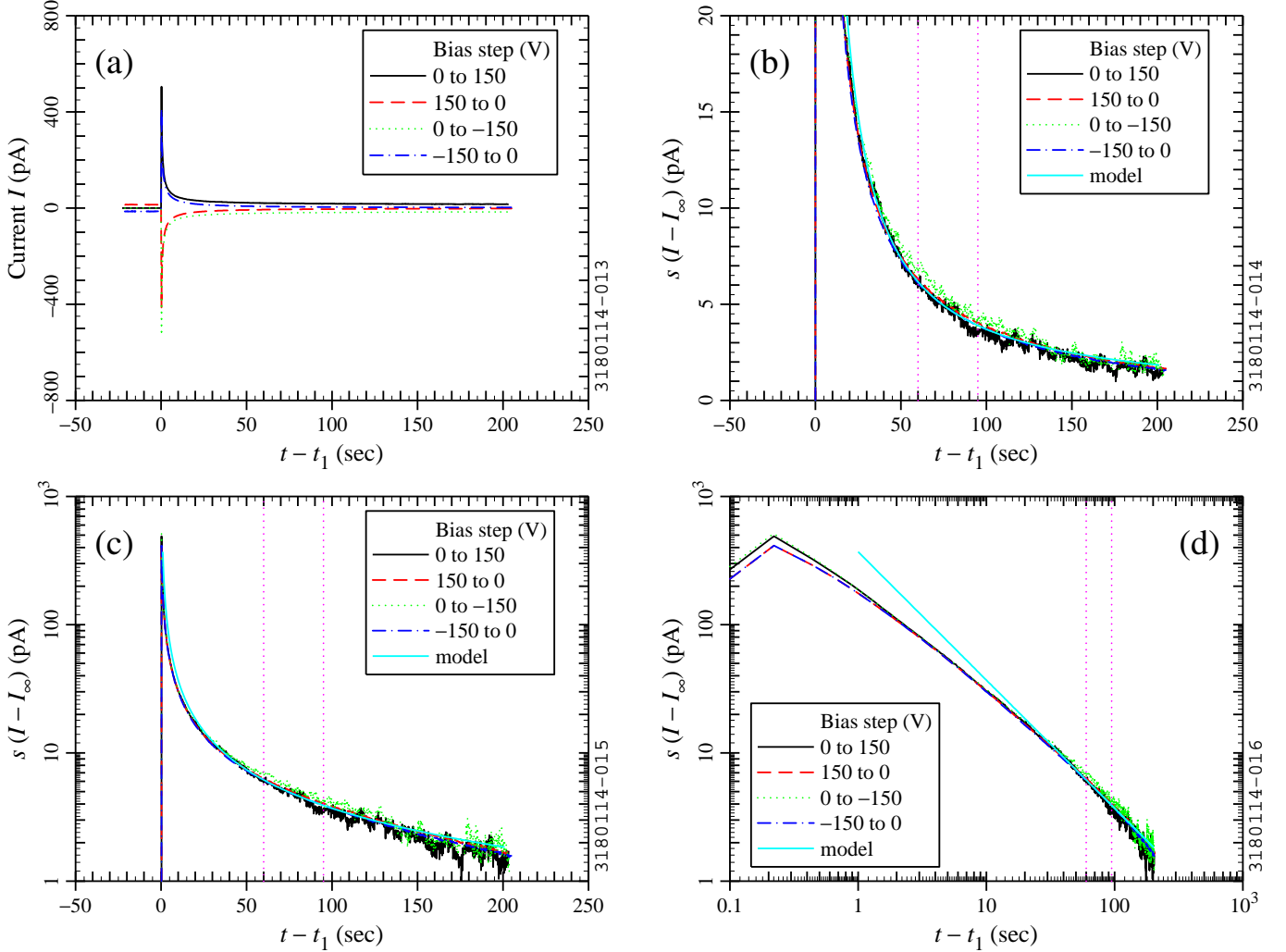


**Figure 22.** (a) Measured current as a function of time for the  $45^\circ$  SEY station with a step in the sample bias at time  $t_1$ . Measured current as a function of time with subtraction of the steady state current  $I_\infty$  and adjustment of the sign ( $s = \pm 1$ ), with (b) linear, (c) linear-log, and (d) log-log scale. The values of  $I_\infty$  are 15 pA, 0, -14 pA, and 1 pA, in the same order as given in the legend. The solid cyan curve represents the model described in the text. The dotted vertical lines indicate the time range of interest for SEY measurements with a double scan.

$R_s$  is small compared to the resistance  $R_{||}$  to ground, the sample bias approaches the power supply voltage in steady state. In the SEY measurements with a double scan, however, the bias is switched from low to high after 60 seconds and from high to low after 95 seconds. Figure 23 indicates that these times are not long enough for the system to reach steady state completely. We do not attempt to account for the possibility of “long-term memory” with the semi-empirical model, as we found that the simple version is able to correct for the transient effects reasonably well. Typical leakage scans show some transient behaviour during the first few iterations (as was seen in Figure 15); it is possible that a more complete model would be able to predict these effects at least in part. The approach we have taken is to keep the model relatively simple and scan the leakage with enough iterations for the initial effects to settle down. Additionally, we make sure to set the bias to -20 V before starting a leakage or SEY scan, so that all of the bias steps are between that same voltages (as the initial step in the leakage and SEY

scans is to set the bias to +150 V to measure  $I_p$ ).

The fact that we are accounting for the active response of the picoammeter in an empirical way brings the question of how applicable the model is for different situations. In particular, when the electron gun is turned on, the magnitude of the picoammeter current is generally larger than it is for the leakage measurements. To check whether the electron gun affects the transient response of the system, we did additional measurements of the sample current as a function of time after a bias step with the electron gun on. We used an Al sample in the off-line station; we set the current for  $I_p \approx 180$  pA with  $K_g = 300$  eV. We found that  $I(t) - I_\infty$  as a function of time after a bias step (between -20 V and +150 V) was very similar with the electron gun on and off, although  $I_\infty$  was quite different between the 2 cases. We inferred from these measurements that the picoammeter response is not qualitatively different between the leakage scans and the SEY scans, and that it is therefore reasonable to apply the semi-empirical model to correct for transient effects in the

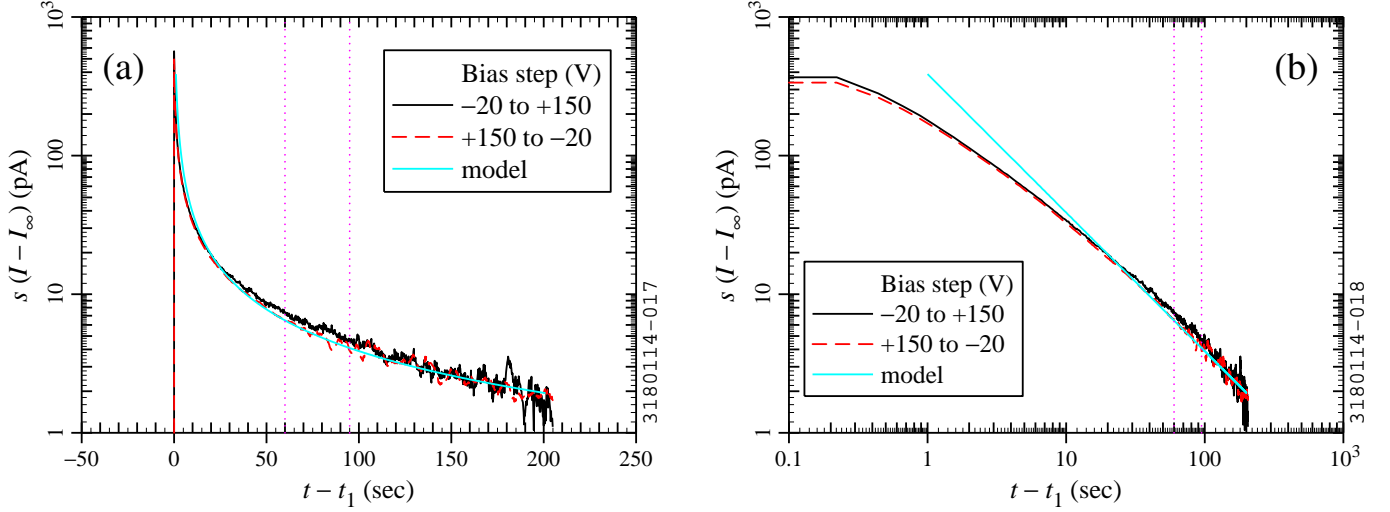


**Figure 23.** Measured current as a function of time for the 45° SEY station with a step in the sample bias at time  $t_1$  between  $-20$  V and  $+150$  V, with (a) linear-log, and (b) log-log scale. The approximate step time  $t_1$  is subtracted from  $t$ . The steady state current  $I_\infty$  is subtracted from  $I(t)$  and the sign is adjusted ( $s = \pm 1$ ) for comparison purposes. The values of  $I_\infty$  are 15 pA and  $-2$  pA. The solid cyan curve represents the model described in the text. The dotted vertical lines indicate the time range of interest for SEY measurements with a double scan.

SEY measurements.

### D.3. Inferring Model Parameters from a Leakage Scan

Equation (7) has two unknown parameters:  $\Gamma_{||}$  and  $R_{||}$ . It is straightforward to infer these parameters from a measurement of the current as a function of time after stepping the bias (with known values of initial bias  $V_0$ , final bias  $V_2$ , and step time  $t_1$ ), as illustrated in Figure 22 above.

However, our measurements have indicated that the leakage current can vary by a small amount from day to day. As described in Section 5.5, this led us to develop a procedure in which we measure the leakage current prior to each SEY measurement, switching between positive and negative sample bias in the same way as is done for the SEY measurements. We denote the positive and negative sample biases as  $V_{hi}$  and  $V_{lo}$  (typically  $V_{hi} = +150$  V and  $V_{lo} = -20$  V, as described in the text). Our procedure is as follows:

**Step 1** We step the bias up from  $V_{lo}$  to  $V_{hi}$  at time  $t_1 = t_{up}$ , wait for time  $\Delta t_{up}$ , and measure the current:

$$I_{pl} = I(t = t_{up} + \Delta t_{up}) . \quad (8)$$

**Step 2** We step the bias down from  $V_{hi}$  to  $V_{lo}$  at time  $t_{down}$ , wait for time  $\Delta t_{down}$ , and measure the current:

$$I_{tl} = I(t = t_{down} + \Delta t_{down}) . \quad (9)$$

**Step 3** We infer the model parameters ( $\Gamma_{||}$ ,  $R_{||}$ ) from  $I_{pl}$  and  $I_{tl}$ .

**Step 4** We use the model parameters to correct the values of  $I_t$  and  $I_p$  measured in the SEY scan.

Note that  $I_{pl}$  is the leakage current with the sample bias used to measure  $I_p$  and  $I_{tl}$  is the leakage current with the bias for measuring  $I_t$ . Likewise,  $\Delta t_{up}$  and  $\Delta t_{down}$  represent the waiting

times between the change of bias and the measurement of  $I_p$  and  $I_t$ , respectively. As indicated above, for one grid point,  $\Delta t_{up} = \Delta t_{down} = 60$  seconds typically; for multiple grid points, we established the convention of using the middle grid point of the first array, so  $\Delta t_{down} \approx 69$  seconds.

As described in Section 5.5, the leakage scan is done in the same way as the SEY scan, so that we typically alternate Step 1 and Step 2 over 16 iterations, and use the average values, discounting initial transients.

For Step 3, we need to be able to infer the model parameters  $\Gamma_{||}$  and  $R_{||}$  from the measured currents  $I_{pl}$  and  $I_{tl}$ . Substituting the appropriate values of  $t_1$ ,  $t$ ,  $V_0$ , and  $V_2$  into Equation (7) for Step 1 and Step 2 gives

$$I_{pl} = \Gamma_{||} \left( \frac{V_{hi} - V_{lo}}{\Delta t_{up}} \right) + \frac{V_{hi}}{R_{||}} \quad (10)$$

$$I_{tl} = \Gamma_{||} \left( \frac{V_{lo} - V_{hi}}{\Delta t_{down}} \right) + \frac{V_{lo}}{R_{||}} \quad (11)$$

With 2 equations and 2 unknowns, we can solve for the model parameters  $\Gamma_{||}$  and  $R_{||}$ :

$$\Gamma_{||} = \frac{V_{lo}I_{pl} - V_{hi}I_{tl}}{(V_{hi} - V_{lo}) \left( \frac{V_{lo}}{\Delta t_{up}} + \frac{V_{hi}}{\Delta t_{down}} \right)} \quad (12)$$

$$R_{||} = \frac{V_{hi}\Delta t_{up} + V_{lo}\Delta t_{down}}{I_{pl}\Delta t_{up} + I_{tl}\Delta t_{down}} \quad (13)$$

Thus, in Step 3, we use Equations (12) and (13) to calculate  $\Gamma_{||}$  and  $R_{||}$  for a given leakage scan. Then, in Step 4, we use Equation (7) to calculate the leakage current at the time of each  $I_p$  and  $I_t$  measurement in the corresponding SEY scan, setting  $t - t_1$  equal to the time elapsed since the last change in sample bias, with appropriate values for the initial bias ( $V_0$ ) and final bias ( $V_2$ ). We subtract the leakage current from each of the current measurements of the SEY scan in order to calculate the corrected SEY.

## Appendix E. Leakage Current Measurements

In the effort to mitigate leakage current while preparing for Phase II, leakage current measurements with and without mitigation were done in parallel with changes to the hardware and data acquisition procedure. Some of the measurements without mitigation were repeated in Phase IIb to get a better understanding of the SEY stations' behaviour in their final hardware state, as will be discussed in [Section E.1](#). The leakage measurements during Phase II allowed us to get a more complete picture of the leakage current stability with mitigation, as will be discussed in [Section E.2](#).

### E.1. Unmitigated Leakage Current: Correlation with Humidity; Time Dependence

To better quantify the leakage current without mitigation from the dry nitrogen gas blanket, we turned off the gas flow to the off-line SEY station and did measurements at various humidities. The humidity was set by the outside air conditions as modified by the climate control system. We measured the humidity using a portable hygrometer.<sup>17</sup> Over several weeks, the relative humidity varied between 9% and 46%.

[Figure 24a](#) shows the measured leakage current ( $I_{leak}$ ) as a function of relative humidity for  $V_b = 150$  V and  $-20$  V. For relative humidities in excess of about 30%, the leakage current increases rapidly, changing by more than a factor of 10 between the lowest and highest humidities. For relative humidities below 30% or so, the leakage current is low, though it still shows some variation. Some of this variation is due to not waiting long enough after a change of bias (referring back to the leakage model of [Section D.1](#), ideally we should have  $I_{leak} = I_\infty$ , but we waited for 1 to 6 minutes after setting the bias, rather than an infinite time). The low-humidity measurements may also be showing some intrinsic variability in the electrical properties of the ceramic breaks and stand-offs. In some of the repeated low-current measurements with  $V_b = -20$  V, we observed that the initial measurement had more leakage current than subsequent measurements made after switching the bias to  $+150$  V and back, which, as mentioned in [Section 5.5](#), may be due to some insulator conditioning effects (there is more noise at the lowest currents as well).

In [Figure 24b](#), we calculate the resistance to ground ( $R_{leak}$ ) from the measured leakage current. The calculated values of  $R_{leak}$  for positive and negative bias are roughly consistent; again, referring back to the model of [Section D.1](#), we should ideally have  $R_{leak} = R_{||}$ , but we can expect some difference since our wait time was finite. The highest values of  $R_{leak}$  are in the range of 10 to 20 T $\Omega$ , consistent with the values inferred for  $R_{||}$  in [Appendix D](#) (as well as [Section E.2](#) below). Hence, under low humidity conditions, the dry nitrogen gas blanket is probably not required.

[Figure 24](#) shows that the leakage correction will be large for SEY measurements with low  $I_p$  in a humid environment

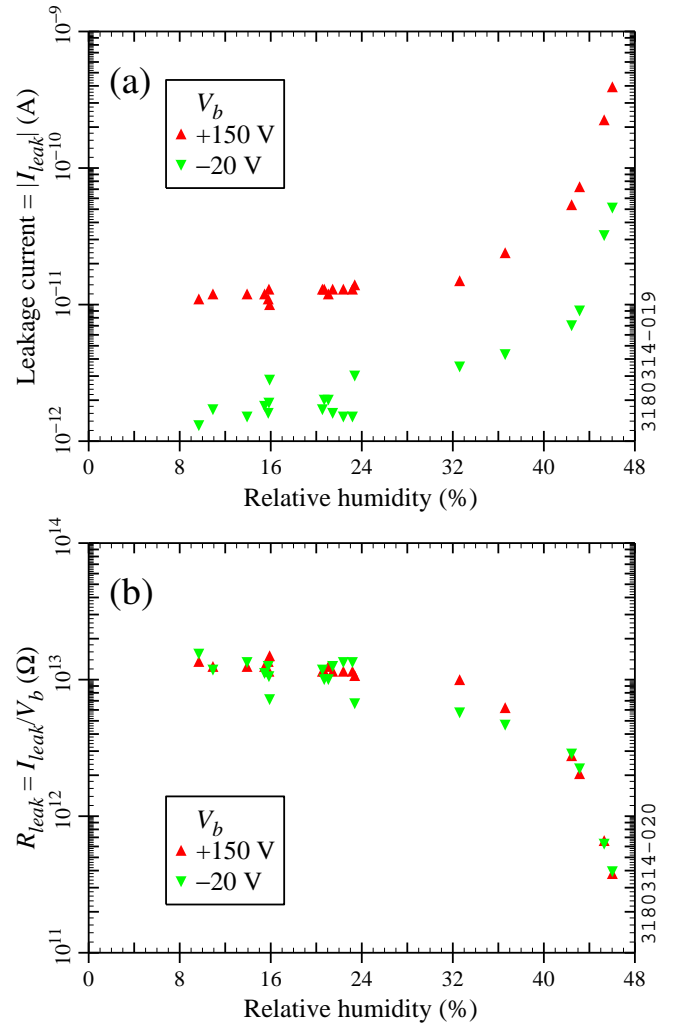


**Figure 24.** Leakage measurements on the off-line SEY station without nitrogen gas flow: (a) leakage current as a function of humidity for positive and sample negative bias; (b) resistance to ground inferred from the leakage current. The temperature was between 21.5 and 23.5°C.

without a gas blanket. For example, with 46% relative humidity, the leakage current with  $V_b + 150$  V exceeds our nominal Phase II value of  $I_p = 200$  pA. The leakage current could be even higher: during the preparations for Phase II, leakage current measurements were done at relative humidities of up to 54%. The corresponding value of  $R_{leak}$  is of order  $2 \cdot 10^{10}$   $\Omega$ ; at this humidity level, the leakage current exceeds even the nominal value of  $I_p = 2$  nA used for Phase I SEY measurements.

Beyond the problem of high leakage current, there is the problem of leakage current stability. For relative humidities above 35% or so, [Figure 24](#) shows that a small change in humidity produces a large change in leakage current. This implies that SEY measurements with low  $I_p$  in a humid environment without a gas blanket are likely to have large systematic errors if there are small variations in the humidity over the course of the measurement. This problem is illustrated by [Figure 25](#), which shows leakage scans done on the off-line SEY station without gas flow, at low and medium ambient humidity. Three leakage scans were done for each humidity level, for a total

<sup>17</sup>Chilled mirror hygrometer, Model 4189, Control Company, Friendswood, TX.



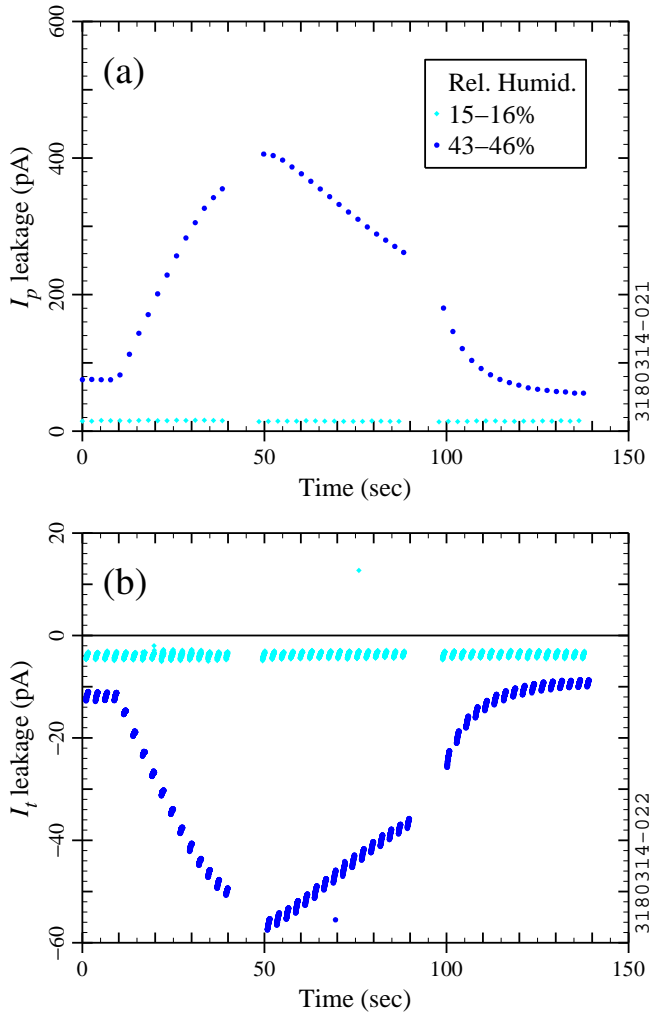


**Figure 25.** Leakage scans on the off-line SEY station without nitrogen gas flow at different ambient humidities: (a) leakage measurements with  $V_b = +150$  V for  $I_p$  correction; (b) repeated leakage measurements with  $V_b = -20$  V for  $I_t$  correction. The temperature was between 21.5 and 23°C.

measurement time of about 140 minutes (which is a bit longer than the 110 minutes needed for a Phase IIb SEY scan). In the low humidity measurements (shown in light blue), the relative humidity decreased from 15.9% to 15.5% over the course of the scans. The leakage current remains low and stable; the behaviour is similar to scans with the nitrogen gas blanket. In the measurements with high relative humidity (dark blue), the relative humidity was initially 43.1%, increasing to 46.0% in the first scan, decreasing to 45.3% in the second scan, and further decreasing to 42.5% in the last scan. Correspondingly, the leakage current varies by about a factor of 4 over the course of the measurement. These measurements support our inference that measurements in a humid environment are prone to poor leakage current stability. Such variation in the leakage current during an SEY scan would introduce large errors in the results.

We conclude that, in a dry environment in which the relative humidity remains below 30%, the leakage current for our SEY stations is relatively stable, and a nitrogen gas blanket is not needed. If the relative humidity can exceed 30%, a dry nitrogen

blanket is useful to ensure low and stable leakage current. However, a dry environment may not remove the need to measure the leakage current in conjunction with SEY measurements; even with a nitrogen blanket, we found that it is necessary to measure the leakage current, as will be discussed in the next section.

## E.2. Mitigated Leakage Current: Long-Term Trends

As described in Section 5.4, we use a nitrogen gas blanket to shield the SEY stations' ceramic breaks from ambient moisture in Phase II. In addition to using this leakage mitigation blanket, we do a leakage scan on both in-situ SEY stations prior to each SEY scan, as discussed in Section 5.5. Figure 26a shows the measured leakage currents during Phase II. The measurements were done over approximately 2 years and 5 months, starting on 27 September 2011 (time = 0) and ending on 25 February 2014 (time = 882 days). Using the procedure and notation of Section D.3, the values labelled  $I_{pl}$  were measured with a bias of  $V_{hi} = +150$  V; the values labelled  $I_{tl}$  were measured with a bias of  $V_{lo} = -20$  V. As can be seen in Figure 26a, the leakage current has varied by roughly a factor of 2 over the time of Phase II measurements. However, the leakage current does not increase or decrease steadily, as we would expect if the ceramic was deteriorating or cleaning itself up. The leakage current changes enough over time to make repeated leakage scans necessary—a constant-leakage assumption would introduce significant systematic errors into the SEY calculation.

Although the leakage currents do not show a clear seasonal dependence, they do not vary randomly. Figure 26a suggests that the leakage current tends to be higher when the accelerator is running and lower during summer and winter down periods. One thing that changes significantly between high-current operation and down periods is the air temperature in the tunnel (including the L3 area where the SEY stations are located). This is illustrated in Figure 26b, which shows the air temperature measured with thermocouple gauges at two locations in the tunnel (40E is approximately 10 m East of the L3 area and 40W is approximately 10 m West of L3). The air temperature increases by about 8°C when CHSS currents are stored due to ohmic losses in the magnets and synchrotron radiation power. Comparison of Figure 26a and Figure 26b shows that the leakage current and the tunnel temperature are indeed correlated. This correlation could come about if the leakage properties of the ceramic or stand-offs are temperature-dependent, if the moisture content of the nitrogen gas blanket is temperature-sensitive, or through some other mechanism.

As discussed in Section 5.6, the Phase II measurement procedure is such that the waiting time after a bias change is not long enough for the current to reach its steady state value. As a result, the leakage current values in Figure 26a are affected by the waiting time. The wait time for the  $I_{pl}$  measurement ( $\Delta t_{up}$ ) was about 60 s throughout Phase II. As discussed in Section D.3, the  $I_{tl}$  wait time ( $\Delta t_{down}$ ) increased from about 60 s to about 69 s as we increased the number of grid points in Phase II. To remove the effect of the transient current, we can express the leakage current in terms of the leakage model parameters of Equation (7):  $R_{||}$  (resistance to ground) and  $\Gamma_{||}$  (the capacitance-like parameter).

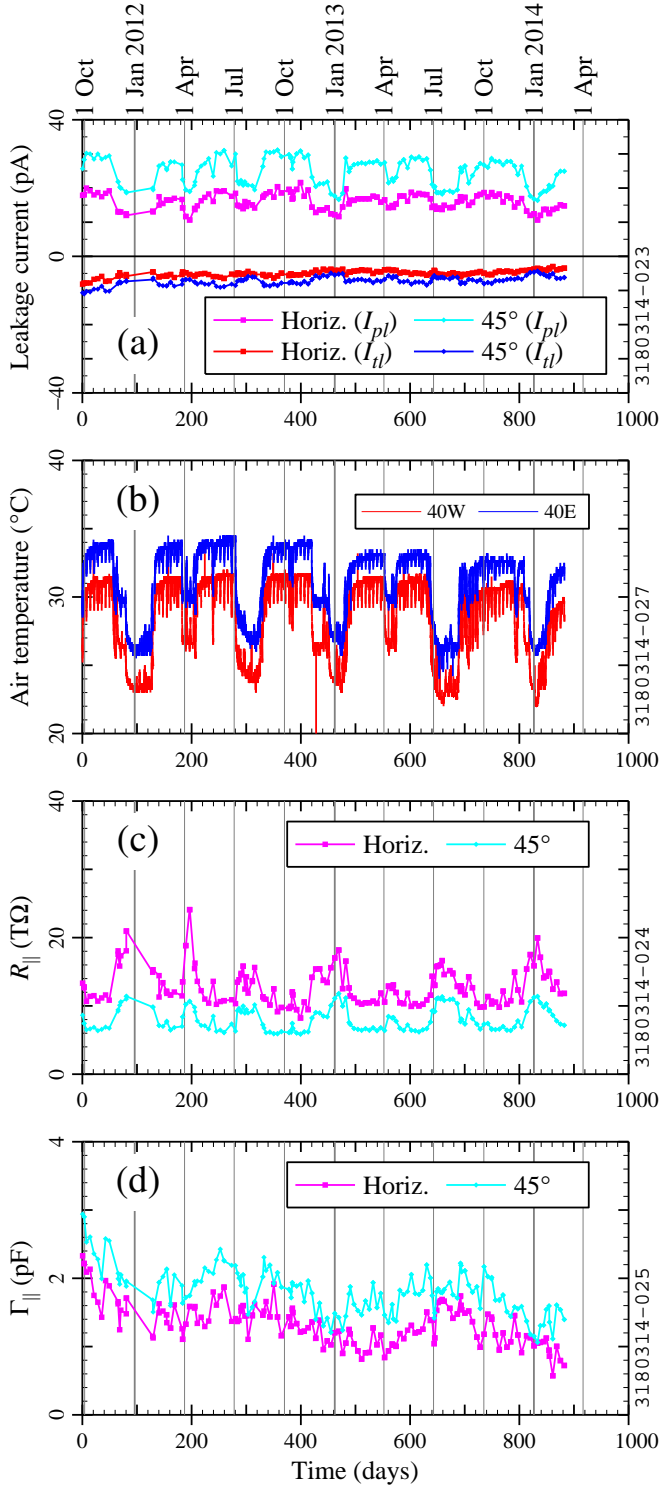


**Figure 26.** Comparison of long-term trends: (a) measured leakage currents, (b) tunnel air temperature, (c, d) leakage model parameters as a function of time. The gray lines correspond to quarterly calendar dates.

Figure 26c and Figure 26d show the model parameters for Phase II. These are calculated from the measured leakage currents of Figure 26a using the procedure of Section D.3. The resistance to ground varies between 5 TΩ and 25 TΩ, and shows a clear inverse correlation with the measured leakage currents, as one would expect;  $\Gamma_{||}$  also shows a time dependence, though it is more difficult to interpret. Figure 26d suggests that  $\Gamma_{||}$  might have some seasonal correlation and possibly a slight downward trend. We would not expect the capacitance to ground to vary significantly over time—the variation in  $\Gamma_{||}$  might be an artifact of the semi-empirical nature of the model for the transient response of the system.

## Appendix F. Inter-System Timing for Simultaneous SEY Scans

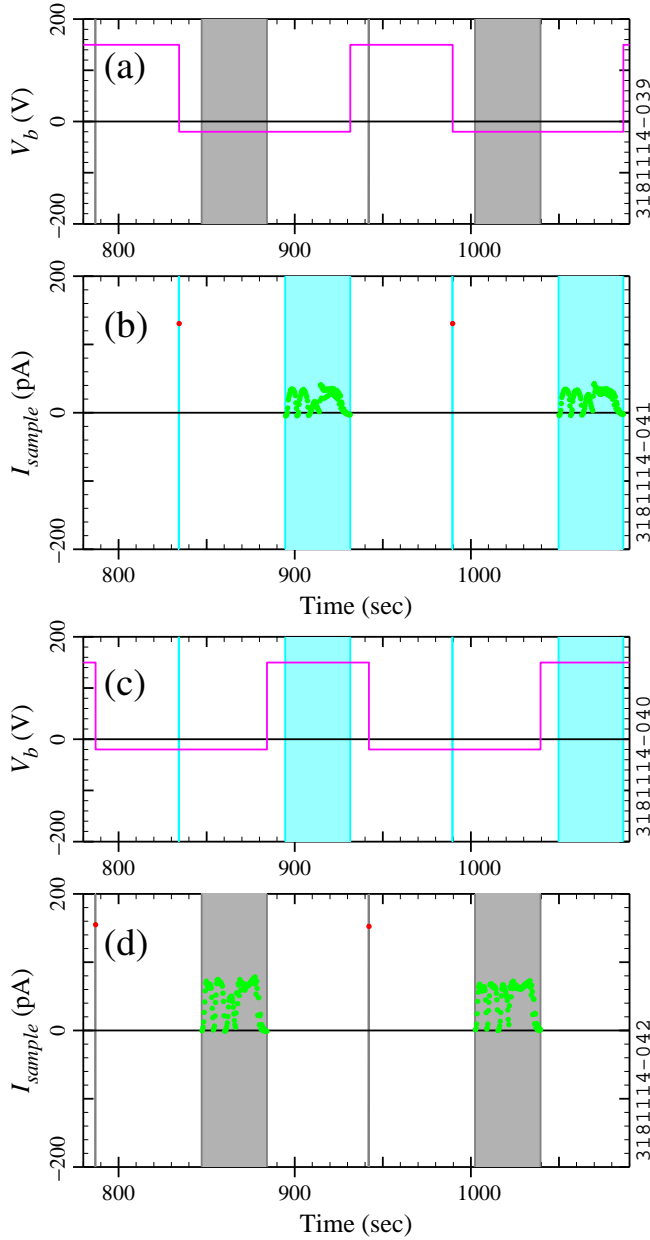
As discussed in Section 5.10, a bias change for one station produces a current spike for the other station, and hence it is important to ensure that bias changes do not happen when we are measuring the current. Timing details for the case of Phase IIb parameters are provided in this section.

Figure 27 shows an example of simultaneous SEY scans with both stations using Phase IIb parameters. Figure 27a shows the bias on the 45° sample as a function of time. A time  $t_{bw} = 60$  s after a change in bias, the 45° sample current is measured, as shown in Figure 27b. The  $I_p$  measurements are done once per energy iteration (red markers), while  $I_t$  is measured for 120 grid points (green markers). The  $I_t$  values vary between 0 and 40 pA as a function of grid point for the 45° sample in this example.

Figure 27c shows the bias on the horizontal sample as a function of time. To ensure that there is no cross-talk, the bias on the horizontal sample must be constant during a “quiet zone” when current measurements are done on the 45° sample, indicated by light blue shading in Figure 27b and Figure 27c. A time  $t_{bw}$  after a change in bias on the horizontal sample, current measurements are done, as shown in Figure 27d. The bias on the 45° sample must be constant when current measurements are done on the horizontal sample, indicated by gray shading in Figure 27d and Figure 27a. The best-case scenario is a start delay of about 47 s between the two systems, which is the case shown in Figure 27. As can be seen, with this start delay, the timing margin is about  $\pm 12$  s. (For high definition scans, the  $I_t$  measurements take 118 s, so measurements on the horizontal and 45° samples are done sequentially instead of in parallel.)

## References

- [1] K. Harkay, “Electron Cloud Observations: A Retrospective,” in *Proceedings of ELOUD 2004: 31st ICFA Advanced Beam Dynamics Workshop on Electron-Cloud Effects*, Napa, CA, M. Furman, S. Henderson & F. Zimmerman, Eds., CERN, Geneva, Switzerland (2004), CERN-2005-001, p. 9–13.
- [2] K. C. Harkay & R. A. Rosenberg, “Properties of the Electron Cloud in a High-Energy Positron and Electron Storage Ring,” *Phys. Rev. ST Accel. Beams* **6**, 034402 (Mar. 2003).
- [3] J. Q. Wang *et al.*, “Electron Cloud Instability Studies in the Beijing Electron Positron Collider,” *Phys. Rev. ST Accel. Beams* **7**, 094401 (Sep. 2004).
- [4] T. Holmquist & J. T. Rogers, “A Trapped Photoelectron Instability in Electron and Positron Storage Rings,” *Phys. Rev. Lett.* **79**, p. 3186–3189 (Oct. 1997).



**Figure 27.** Inter-system timing schematic for SEY scans in Phase IIb: (a) bias and (b) current measurements for 45° system; (c) bias and (d) current measurements for horizontal system. Two iterations in the energy scan are shown. Red markers:  $I_p$  measurements; green markers:  $I_t$  measurements. Shaded areas: “quiet zones” for current measurements (light blue: times of current measurements on 45° sample; gray: times of current measurements on horizontal sample).

[5] M. Tobiyama *et al.*, “Coupled Bunch Instability Caused by an Electron Cloud,” *Phys. Rev. ST Accel. Beams* **9**, 012801 (Jan. 2006).  
 [6] M. Izawa, Y. Sato & T. Toyomasu, “The Vertical Instability in a Positron Bunched Beam,” *Phys. Rev. Lett.* **74**, p. 5044–5047 (Jun. 1995).  
 [7] W. Fischer *et al.*, “Electron Cloud Observations and Cures in the Relativistic Heavy Ion Collider,” *Phys. Rev. ST Accel. Beams* **11**, 041002 (Apr. 2008).  
 [8] R. Capii *et al.*, “Electron Cloud Buildup and Related Instability in the CERN Proton Synchrotron,” *Phys. Rev. ST Accel. Beams* **5**, 094401 (Sep. 2002).  
 [9] R. J. Macek *et al.*, “Electron Cloud Generation and Trapping in a

Quadrupole Magnet at the Los Alamos Proton Storage Ring,” *Phys. Rev. ST Accel. Beams* **11**, 010101 (Jan. 2008).  
 [10] J. A. Holmes *et al.*, “Computational Beam Dynamics Studies of Collective Instabilities Observed in SNS,” in *Proceedings of the 2008 European Particle Accelerator Conference, Genoa, Italy*, EPS-AG (2008), p. 1640–1642.  
 [11] D. R. Grosso *et al.*, “Effect of the Surface Processing on the Secondary Electron Yield of Al Alloy Samples,” *Phys. Rev. ST Accel. Beams* **16**, 051003 (May 2013).  
 [12] A. Kulikov *et al.*, “The Electron Cloud Instability at PEP-II,” in *Proceedings of the 2001 Particle Accelerator Conference, Chicago, IL*, P. Lucas & S. Webber, Eds., IEEE (2001), p. 1903–1905.  
 [13] S. Casalbuoni *et al.*, “Can Electron Multipacting Explain the Pressure Rise in a Cold Bore Superconducting Undulator?” *Phys. Rev. ST Accel. Beams* **13**, 073201 (Jul. 2010).  
 [14] F. Zimmermann, “Electron-Cloud Effects in Past & Future Machines—Walk through 50 Years of Electron-Cloud Studies,” in *Proceedings of ECLLOUD 2012: Joint INFN-CERN-EuCARD-AccNet Workshop on Electron-Cloud Effects, La Biodola, Elba, Italy*, R. Cimino, G. Rumolo & F. Zimmermann, Eds., CERN, Geneva, Switzerland (2013), CERN-2013-002, p. 9–17.  
 [15] Y. Suetsugu *et al.*, “Design and Construction of the SuperKEKB Vacuum System,” *J. Vac. Sci. Technol. A* **30**, 031602 (May 2012).  
 [16] M. T. F. Pivi *et al.*, “Recommendation for the Feasibility of More Compact LC Damping Rings,” in *Proceedings of the 2010 International Particle Accelerator Conference, Kyoto, Japan*, ACFA (2010), p. 3578–3580.  
 [17] G. Rumolo, W. Bruns & Y. Papaphilippou, “Electron Cloud Build Up and Instability in the CLIC Damping Rings,” in *Proceedings of the 2008 European Particle Accelerator Conference, Genoa, Italy*, EPS-AG (2008), p. 661–663.  
 [18] M. A. Furman, “Electron Cloud Effects in Accelerators,” in *Proceedings of ECLLOUD 2012: Joint INFN-CERN-EuCARD-AccNet Workshop on Electron-Cloud Effects, La Biodola, Elba, Italy*, R. Cimino, G. Rumolo & F. Zimmermann, Eds., CERN, Geneva, Switzerland (2013), CERN-2013-002, p. 1–8.  
 [19] M. A. Palmer *et al.*, “The Conversion and Operation of the Cornell Electron Storage Ring as a Test Accelerator (CesrTA) for Damping Rings Research and Development,” in *Proceedings of the 2009 Particle Accelerator Conference, Vancouver, BC* (2009), p. 4200–4204.  
 [20] D. Rubin, “CesrTA Program Overview,” in *Proceedings of ECLLOUD 2010: 49th ICFA Advanced Beam Dynamics Workshop on Electron Cloud Physics, Ithaca, NY*, K. Smolenski, Ed., Cornell University, Ithaca, NY (2013), p. 30–36.  
 [21] “The CESR Test Accelerator Electron Cloud Research Program: Phase I Report,” Tech. Rep. CLNS-12-2084, LEPP, Cornell University, Ithaca, NY (Jan. 2013).  
 [22] J. R. Calvey *et al.*, “Measurement and Modeling of Electron Cloud in a Field Free Environment Using Retarding Field Analyzers,” *Phys. Rev. ST Accel. Beams* **17**, 061001 (Jun. 2014).  
 [23] J. A. Crittenden *et al.*, “Shielded Button Electrodes for Time-Resolved Measurements of Electron Cloud Buildup,” *Nucl. Instrum. Methods Phys. Res. A* **749**, p. 42–46 (Jun. 2014).  
 [24] J. P. Sikora *et al.*, “Electron Cloud Density Measurements in Accelerator Beam-Pipe Using Resonant Microwave Excitation,” *Nucl. Instrum. Methods Phys. Res. A* **754**, p. 28–35 (Aug. 2014).  
 [25] Y. Li *et al.*, “Electron Cloud Diagnostic Chambers with Various EC-Suppression Coatings,” in *IPAC2013: Proceedings of the 4th International Particle Accelerator Conference, Shanghai, China*, Z. Dai *et al.*, Eds., JACoW (2013), p. 3496–3498.  
 [26] R. A. Rosenberg *et al.*, “X-Ray Photoelectron Spectroscopy and Secondary Electron Yield Analysis of Al and Cu Samples Exposed to an Accelerator Environment,” *J. Vac. Sci. Technol. A* **21**, p. 1625–1630 (Sep. 2003).  
 [27] V. Baglin *et al.*, “The Secondary Electron Yield of Technical Materials and Its Variation with Surface Treatments,” in *Proceedings of the 2000 European Particle Accelerator Conference, Vienna, Austria* (2000), p. 217–221.  
 [28] J. M. Jimenez *et al.*, “Electron Cloud with LHC-Type Beams in the SPS: A Review of Three Years of Measurements,” in *Mini Workshop on Electron Cloud Simulations for Proton and Positron Beams—ECLLOUD’02, Geneva, Switzerland*, G. Rumolo & F. Zimmermann, Eds., CERN,

- Geneva, Switzerland (2002), CERN-2002-001, p. 17–28.
- [29] B. Henrist *et al.*, “The Variation of the Secondary Electron Yield and of the Desorption Yield of Copper under Electron Bombardment: Origin and Impact on the Conditioning of LHC,” in *Proceedings of the 2002 European Particle Accelerator Conference, Paris, France*, EPS-IGA/CERN (2002), p. 2553–2555.
  - [30] C. Yin Vallgren *et al.*, “Amorphous Carbon Coatings for the Mitigation of Electron Cloud in the CERN Super Proton Synchrotron,” *Phys. Rev. ST Accel. Beams* **14**, 071001 (Jul. 2011).
  - [31] C. Yin Vallgren *et al.*, “Performance of Carbon Coating for Mitigation of Electron Cloud in the SPS,” in *Proceedings of the 2011 International Particle Accelerator Conference, San Sebastián, Spain*, EPS-AG (2011), p. 1590–1592.
  - [32] S. Kato & M. Nishiwaki, “In-Situ SEY Measurements at KEKB Positron Ring and Comparison with Laboratory Experiments,” in *Proceedings of ECLLOUD 2007: International Workshop on Electron-Cloud Effects, Daegu, Korea*, H. Fukuma, E. S. Kim & K. Ohmi, Eds., KEK, Tsukuba, Japan (2007), KEK Proceedings 2007-10, p. 72–75.
  - [33] S. Kato & M. Nishiwaki, “Study on Graphitization and DLC Coating on KEKB LER Chambers,” Presented at AEC 2009: Workshop on Anti e-Cloud Coatings, Geneva, Switzerland, October 2009, Talk 24.
  - [34] M. T. F. Pivi *et al.*, “Experimental Observations of In Situ Secondary Electron Yield Reduction in the PEP-II Particle Accelerator Beam Line,” *Nucl. Instrum. Methods Phys. Res. A* **621**, p. 47–56 (Sep. 2010).
  - [35] R. Cimino *et al.*, “Can Low-Energy Electrons Affect High-Energy Physics Accelerators?” *Phys. Rev. Lett.* **93**, 014801 (Jul. 2004).
  - [36] R. Lariciprete *et al.*, “Secondary Electron Yield of Cu Technical Surfaces: Dependence on Electron Irradiation,” *Phys. Rev. ST Accel. Beams* **16**, 011002 (Jan. 2013).
  - [37] M. Nishiwaki & S. Kato, “Influence of Electron Irradiation and Heating on Secondary Electron Yields from Non-Evaporable Getter Films Observed with In Situ X-Ray Photoelectron Spectroscopy,” *J. Vac. Sci. Technol. A* **25**, p. 675–679 (Jul. 2007).
  - [38] M. Nishiwaki & S. Kato, “Measurement of Secondary Electron Yields from Bulky and Coated Materials for Beam Ducts,” in *Proceedings of ECLLOUD 2007: International Workshop on Electron-Cloud Effects, Daegu, Korea*, H. Fukuma, E. S. Kim & K. Ohmi, Eds., KEK, Tsukuba, Japan (2007), KEK Proceedings 2007-10, p. 82–85.
  - [39] M. Nishiwaki & S. Kato, “Study on Secondary Electron Emission from Carbon Materials,” *Shinku: J. Vac. Soc. Jpn.* **48**, p. 118–120 (2005).
  - [40] R. E. Kirby & F. K. King, “Secondary Electron Emission Yields from PEP-II Accelerator Materials,” *Nucl. Instrum. Methods Phys. Res. A* **469**, p. 1–12 (Aug. 2001).
  - [41] F. Le Pimpec *et al.*, “Properties of TiN and TiZrV Thin Film as a Remedy Against Electron Cloud,” *Nucl. Instrum. Methods Phys. Res. A* **551**, p. 187–199 (Jul. 2005).
  - [42] F. Le Pimpec *et al.*, “Electron Conditioning of Technical Aluminium Surfaces: Effect on the Secondary Electron Yield,” *J. Vac. Sci. Technol. A* **23**, p. 1625–1630 (Nov. 2005).
  - [43] R. E. Kirby, “Instrumental Effects in Secondary Electron Yield and Energy Distribution Measurements,” in *Proceedings of ECLLOUD 2004: 31st ICFA Advanced Beam Dynamics Workshop on Electron-Cloud Effects, Napa, CA*, M. Furman, S. Henderson & F. Zimmerman, Eds., CERN, Geneva, Switzerland (2004), CERN-2005-001, p. 107–111.
  - [44] R. E. Kirby, “Artifacts in Secondary Electron Emission Yield Measurements,” Tech. Rep. SLAC-PUB-10541, SLAC, Stanford, CA (Jul. 2004).
  - [45] D. J. Scott *et al.*, “Secondary Electron Yield Measurements of Fermilab’s Main Injector Vacuum Vessel,” in *Proceedings of the 2012 International Particle Accelerator Conference, New Orleans, LA*, IEEE (2012), p. 166–168.
  - [46] M. A. Furman & M. T. F. Pivi, “Probabilistic Model for the Simulation of Secondary Electron Emission,” *Phys. Rev. ST Accel. Beams* **5**, 124404 (Dec. 2002).
  - [47] W. Hartung *et al.*, “In-Situ Measurements of the Secondary Electron Yield in an Accelerator Environment: Instrumentation and Methods,” Submitted to Nucl. Instrum. Methods. Phys. Res. A.
  - [48] J. Kim *et al.*, “In Situ SEY Measurements at CsrTA,” in *Proceedings of ECLLOUD 2010: 49th ICFA Advanced Beam Dynamics Workshop on Electron Cloud Physics, Ithaca, NY*, K. Smolenski, Ed., Cornell University, Ithaca, NY (2013), p. 140–146.
  - [49] J. Kim *et al.*, “In-Situ Secondary Electron Yield Measurement System at CsrTA,” in *Proceedings of the 2011 Particle Accelerator Conference, New York, NY*, IEEE (2011), p. 1253–1255.
  - [50] W. Hartung *et al.*, “Measurements of Secondary Electron Yield of Metal Surfaces and Films with Exposure to a Realistic Accelerator Environment,” in *IPAC2013: Proceedings of the 4th International Particle Accelerator Conference, Shanghai, China*, Z. Dai *et al.*, Eds., JACoW (2013), p. 3493–3495.
  - [51] Y. Suetsugu *et al.*, “Experimental Studies on Grooved Surfaces to Suppress Secondary Electron Emission,” in *Proceedings of the 2010 International Particle Accelerator Conference, Kyoto, Japan*, ACFA (2010), p. 2021–2023.
  - [52] J. J. Scholtz *et al.*, “Description of the Influence of Charging on the Measurement of the Secondary Electron Yield of MgO,” *Appl. Surf. Sci.* **111**, p. 259–264 (Feb. 1997).
  - [53] R. Cimino *et al.*, “Nature of the Decrease of the Secondary-Electron Yield by Electron Bombardment and its Energy Dependence,” *Phys. Rev. Lett.* **109**, 064801 (Aug. 2012).
  - [54] H. L. Curtis, “Insulating Properties of Solid Dielectrics,” *Bull. Bur. Stand. (U. S.)* **11**, p. 359–420 (May 1915).
  - [55] R. F. Field, “The Formation of Ionized Water Films on Dielectrics under Conditions of High Humidity,” *J. Appl. Phys.* **17**, p. 318–325 (May 1946).
  - [56] H. R. Baker & R. N. Bolster, “Surface Electrical Leakage on Insulators and Coatings in the Presence of Moisture Condensation,” *IEEE Trans. Electr. Insul.* **11**, p. 76–80 (Sep. 1976).